

# **THE EFFECT OF IONOSPHERIC SCINTILLATION ON IMAGE RECONSTRUCTION BY SYNTHETIC APERTURE RADIO TELESCOPE**

A Thesis Submitted  
in Partial Fulfilment of the Requirements  
for the Degree of

**MASTER OF TECHNOLOGY**

by

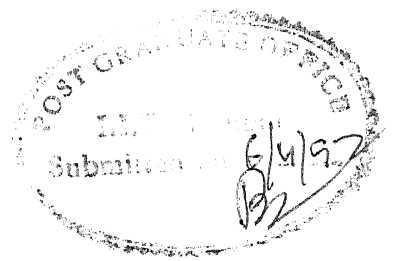
**RAJEEV MAHAJAN**

to the

**DEPARTMENT OF ELECTRICAL ENGINEERING  
INDIAN INSTITUTE OF TECHNOLOGY KANPUR**

**APRIL, 1992**

*Dedicated to my parents  
who gifted me the love for  
learning*



## CERTIFICATE

This is to certify that the work presented in this thesis entitled "THE EFFECT OF IONOSPHERIC SCINTILLATION ON IMAGE RECONSTRUCTION BY SYNTHETIC APERTURE RADIO TELESCOPE" by Rajeev Mahajan has been done under my supervision and it has not been submitted elsewhere for a degree.

*N.C. Mathur*

Dr. N. C. Mathur  
Professor  
Department of Electrical Engineering  
Indian Institute of Technology, Kanpur  
KANPUR - 208 016

6 JUN 1992

CENTRAL LIBRARY  
I I T KANPUR

Acc. No. 4113548

EE-1992-M-MAH-EFF



## ACKNOWLEDGEMENTS

I would like to thank my guide Prof. N.C. Mathur for his valuable time and suggestions which made this thesis possible. Dr. P.K. Pasricha from NPL, Delhi has to be thanked for his patient help during my fortnights stay at NPL for the purpose of getting the WBMOD code working.

The credit for making this thesis presentable in this form goes to Y.P. Singh and Manish who looked after the photography. Harish's knowledge of workstations and Kazmi's dexterity with programming were a great help when the whole world seemed to be on the verge of collapsing. Thanks are also due to a host of my other friends including Pathak, Pillai and Navneet who were somehow or the other associated with this work.

This page would not be complete if I were not to mention Mr. J.P. Gupta who did a very fine job of typing the thesis.

RAJEEV MAHAJAN

---

## ABSTRACT

The radio images reconstructed by using Synthetic Aperture Radio Telescopes are distorted due to the effect of ionospheric irregularities. The effects are especially pronounced at lower frequencies. The effects have been studied for the Giant Metre Wave Radio Telescope (GMRT) being built at Pune, India. GMRT being a metre wave radio telescope is very susceptible to these image distortions due to the effect of the ionospheric irregularities. A new approach to integrate the work of both the astronomers and the propagation community has been tried using the mutual coherence function (MCF). Simulations to study the effects of different parameters like frequency, declination, sun spot number etc. have been carried out. The ionospheric irregularities have been modeled by the WBMOD program for calculation of scintillation indices developed by Fremouw. The effects can be clearly seen in the color coded photographs attached.

## CONTENTS

		<u>PAGE</u>
<b>CHAPTER 1</b>	<b>:</b>	<b>INTRODUCTION</b>
1.1	:	Radio Astronomy 1
1.2	:	Aperture Synthesis 2
1.3	:	Propagation Effects 5
1.4	:	Summary of Present Work 7
<b>CHAPTER 2</b>	<b>:</b>	<b>INTERFEROMETRY AND RADIO IMAGE MAPPING</b>
2.1	:	Interferometry Theory 8
2.2	:	Source Synthesis 13
2.3	:	Two Dimensional Mapping 17
2.4	:	Antenna Spacing Co-ordinates and (u,v) Locii 19
2.5	:	Discrete Fourier Transformation 22
2.6	:	Mutual Coherence Function 27
<b>CHAPTER 3</b>	<b>:</b>	<b>IONOSPHERIC SCINTILLATION AND MUTUAL COHERENCE FUNCTION</b>
3.1	:	Ionospheric Irregularities and Spectra 29
	:	3.1.1 : Correlation function & spectra 31
3.2	:	Optical Path Structure Function 34
3.3	:	MCF and the Structure Function 35
<b>CHAPTER 4</b>	<b>:</b>	<b>DESCRIPTION OF PROGRAM CODE 38</b>

**CHAPTER 5 : RESULTS AND CONCLUSION**

5.1	:	Effect of Size of Source	48
5.2	:	Effect of Declination of Source	50
5.3	:	Effect of Frequency	50
5.4	:	Effect of Right Ascension	50
5.5	:	Effect of Season	51
5.6	:	Effect of Sun Spot Number	51
5.7	:	Conclusion	51

<b>REFERENCES</b>	71
-------------------	----

## LIST OF ILLUSTRATIONS

	<u>PAGE</u>
2.1 : Elementary interferometer	9
2.2 : Point source response of an interferometer with rectangular passband	12
2.3 : Power reception pattern of a typical antenna	14
2.4 : Geometrical relationship between a source under observation $B(\xi, \eta)$ and an interferometer or one antenna pair of an array	18
2.5 : Spacing vector locii in the $u-v$ plane	20
2.6 : The co-ordinate system for the base-line measurement	21
2.7 : Points on a rectangular grid in the $(u,v)$ plane at which the visibility is sampled for use with the discrete Fourier transform	24
2.8 : Rearrangement of a visibility function for input to the discrete Fourier transform	25
3.1 : The geometry of the problem : The thin phase screen approximation	30
3.2 : The spectral density function $Q(q)$	33
4.1 : $W(u,v)$ function	
a) for 327 MHz at $\delta = -30^\circ$	39
b) for 327 MHz at $\delta = 0^\circ$	39
c) for 327 MHz at $\delta = 30^\circ$	39
d) for 327 MHz at $\delta = 60^\circ$	39
e) for 38 MHz at $\delta = 30^\circ$	40
f) for 153 MHz at $\delta = 30^\circ$	40
g) for 233 MHz at $\delta = 30^\circ$	40
h) for 611 MHz at $\delta = 30^\circ$	40
4.2 : Array configuration of giant metre wave radio telescope	43
5.1 : Assumed point source distribution	53
5.2 : Assumed extended gaussian source distribution	54

- 5.3 : a) Plot-B corresponding to plot-A of Fig. 5.1 for 55  
given parameters  
b) Plot-C corresponding to plot-A of Fig. 5.1  
for given parameters
- 5.4 : a) Plot-B corresponding to plot-A of Fig. 5.1 for 56  
given parameters  
b) Plot-C corresponding to plot-A of Fig. 5.1  
for given parameters
- 5.5 : a) Plot-B corresponding to plot-A of Fig. 5.1 for 57  
given parameters  
b) Plot-C corresponding to plot-A of Fig. 5.1  
for given parameters
- 5.6 : a) Plot-B corresponding to plot-A of Fig. 5.1 for 58  
given parameters  
b) Plot-C corresponding to plot-A of Fig. 5.1  
for given parameters
- 5.7 : a) Plot-B corresponding to plot-A of Fig. 5.1 for 59  
given parameters  
b) Plot-C corresponding to plot-A of Fig. 5.1  
for given parameters
- 5.8 : a) Plot-B corresponding to plot-A of Fig. 5.1 for 60  
given parameters  
b) Plot-C corresponding to plot-A of Fig. 5.1  
for given parameters
- 5.9 : a) Plot-B corresponding to plot-A of Fig. 5.1 for 61  
given parameters  
b) Plot-C corresponding to plot-A of Fig. 5.1  
for given parameters
- 5.10 : a) Plot-B corresponding to plot-A of Fig. 5.1 for 55  
given parameters  
b) Plot-C corresponding to plot-A of Fig. 5.1  
for given parameters
- 5.11 : a) Plot-B corresponding to plot-A of Fig. 5.2 for 63  
given parameters  
b) Plot-C corresponding to plot-A of Fig. 5.2  
for given parameters
- 5.12 : a) Plot-B corresponding to plot-A of Fig. 5.2 for 64  
given parameters  
b) Plot-C corresponding to plot-A of Fig. 5.2  
for given parameters

- 5.13 : a) Plot-B corresponding to plot-A of Fig. 5.2 for 65  
given parameters  
b) Plot-C corresponding to plot-A of Fig. 5.2  
for given parameters
- 5.14 : a) Plot-B corresponding to plot-A of Fig. 5.1 for 66  
given parameters  
b) Plot-C corresponding to plot-A of Fig. 5.1  
for given parameters
- 5.15 : a) Plot-B corresponding to plot-A of Fig. 5.1 for 67  
given parameters  
b) Plot-C corresponding to plot-A of Fig. 5.1  
for given parameters
- 5.16 : a) Plot-B corresponding to plot-A of Fig. 5.2 for 68  
given parameters  
b) Plot-C corresponding to plot-A of Fig. 5.2  
for given parameters
- 5.17 : a) Plot-B corresponding to plot-A of Fig. 5.2 for 69  
given parameters  
b) Plot-C corresponding to plot-A of Fig. 5.2  
for given parameters
- 5.18 : a) Plot-B corresponding to plot-A of Fig. 5.2 for 70  
given parameters  
b) Plot-C corresponding to plot-A of Fig. 5.2  
for given parameters

## LIST OF TABLES

			<u>PAGE</u>
4.1	:	The GMRT antenna array co-ordinates in metres	44
0	:	List of various figures and tables for different parameters	48
1	:	dB errors for plots of Fig. 5.3	56
2	:	dB errors for plots of Fig. 5.4	57
3	:	dB errors for plots of Fig. 5.5	58
4	:	dB errors for plots of Fig. 5.6	58
5	:	dB errors for plots of Fig. 5.7	59
6	:	dB errors for plots of Fig. 5.8	60
7	:	dB errors for plots of Fig. 5.9	61
8	:	dB errors for plots of Fig. 5.10	62
9	:	dB errors for plots of Fig. 5.11	63
10	:	dB errors for plots of Fig. 5.12	64
11	:	dB errors for plots of Fig. 5.13	65
12	:	dB errors for plots of Fig. 5.14	66
13	:	dB errors for plots of Fig. 5.15	67
14	:	dB errors for plots of Fig. 5.16	68
15	:	dB errors for plots of Fig. 5.17	69
16	:	dB errors for plots of Fig. 5.18	70



## CHAPTER - 1

### INTRODUCTION

Astronomy is traditionally "looking at the sky" and interpreting the message that starlight brings. But objects in space emit more than ordinary light. They radiate other wavelengths (X-rays, ultraviolet, infrared and radio waves) and most of the exciting astronomical discoveries of the past 20 years - quasars, pulsars, black holes, proof of the Big Bang have been made by studying these other radiations.

#### 1.1 RADIO ASTRONOMY

Radio Astronomy is the "Grand old man" of the new astronomies. X-ray, ultraviolet and infrared radiations are absorbed by Earth's atmosphere, and it is difficult to study them except from high mountains, balloons, rockets or preferably satellites completely above the atmosphere. Radio waves from space do reach the ground, however, so their observations is an easier proposition. Nearly 60 years have passed since cosmic radio waves were first detected, and in that time radio astronomers have overtaken their optical colleagues in many ways. Radio telescopes can now "see" details a thousand times finer than optical astronomers can photograph and the positions of radio sources can be pin pointed to five times the accuracy of optical positions in the sky.

The two major criteria of performance of a telescope are its sensitivity and its resolving power. The first function determines its ability to observe objects otherwise too faint to be seen with the unaided eye. The second function determines telescope's ability to separate sources that would appear as a single source to the naked eye. The theoretical resolving power of a telescope, defined as the smallest angular separation between two sources which can be seen as two distinct sources, is proportional to  $\lambda/D$ , where  $\lambda$  is the wavelength of the radiation and  $D$  is diameter of the aperture.

To obtain a resolution equivalent to that of a 200 inch optical telescope, the diameter of the collecting surface for a radio telescope would be some 150 miles at 1000 MHz.

The skillful applications of the techniques of radio interferometry coupled with the evolution of computer technology, has led to resolving powers that were inconceivable in the early days of radio astronomy. In the past few years radio astronomers have obtained resolutions of 0.0001 arc seconds which constitutes an improvement of some four orders of magnitude over the resolution of earth based optical telescopes.

## 1.2 APERTURE SYNTHESIS AND GMRT

The high resolutions of 0.0001 arc second does not violate the relation  $\lambda/D$ . The requirement of making the aperture  $D$  very large is accomplished by "aperture synthesis", a technique in

which the radio waves collected by two (or more) instruments upto tens, hundreds and even thousands of kilometers apart are recorded simultaneously and subsequently added together. The addition must be done, of course, in a special way; it is necessary to arrange the observations precisely so that the phase relations of radio waves arriving at the telescope participating in the synthesis is preserved.

Since the earth rotates, the relative position of two radio telescopes is continuously changing. As a result the signal intensity at the output of the interferometer passes rapidly through a succession of maxima and minima called interference fringes.

The actual shape of the intensity variations is a sine wave. The amplitude and phase of the sine wave embody information about the structure of the celestial object on a certain angular scale, which depends on the distance between two telescopes as seen from the source. If the distance between the telescopes is changed, one gets a different pattern, which then contains information about the structure of the object on a different angular scale.

It is therefore possible to measure the fringe pattern for a range of telescope separations and so to cover a range of angular scales on the sky. The amplitudes and phases of the fringes, sampled for a large number of separation of the two telescopes are called the visibility function.

This visibility function happens to be the Fourier Transform of the brightness distribution of the source in the sky. Hence if the visibility function is measured for all possible baselines, then, theoretically at least, the brightness distribution can be obtained by Fourier transformation.

In practice it is possible to obtain the fringe pattern for all separation of two telescopes out to a maximum separation,  $D$ . This enables one to obtain the same image that one would get from a single giant telescope of diameter  $D$ . The different baseline separations  $D$  can be obtained either by moving one of the antennas or by having large number of different antennas. When the rotation of the earth is exploited to increase the number of separations, the resulting operation is called earth-rotation aperture synthesis or super synthesis. Most of the large radio telescopes built in the last two decades follow this principle. In India, the Giant Metre-Wave Radio Telescope (GMRT) is being setup at Pune. GMRT will consist of 30 fully steerable 45 m diameter parabolic dishes and is being designed to operate in six separate frequency bands between 38 MHz and 1420 MHz. The GMRT will operate as an "Earth Rotation Synthesis Radio Telescope". Its 30 antennas will form 435 interferometric pairs with the length and orientation of the projected baselines changing continuously with the diurnal rotation of the earth. What makes GMRT unique is the relatively lower frequency range of operation.

### 1.3 PROPAGATION EFFECTS

The fundamental measurements in the aperture synthesis telescope are the amplitude and phase of the fringe visibility. Both of these parameters are affected by the passage of the wave through the earth's atmosphere. The irregular structure of refractive index of the atmosphere causes random variation in amplitude and phase called scintillation. At lower frequencies the scintillation due to the ionosphere are the predominant factors. Since Pune is in the equatorial F-region ionospheric scintillation region, the study of ionospheric scintillation on the reconstructed images becomes important. This thesis tries to address this problem.

When a wave propagates through the ionosphere, there are two major effects that come into play

- i) The regular effects, and
- ii) The irregular effects.

The regular effects are primarily

- a) Refraction, due to change in permittivity which changes regularly with the electron density in the different regions of the ionosphere
- b) Absorption
- c) Faraday rotation which changes the plane of polarisation of the radio wave, and
- d) Introduction of an excess path length.

All these changes are related to the change in permittivity of the ionosphere given by

$$\Delta \epsilon \propto \frac{N_e}{\nu^2} , \quad \begin{array}{l} N_e \rightarrow \text{electron density} \\ \nu \rightarrow \text{frequency} \end{array}$$

Clearly all these effects scale as  $\nu^{-2}$  and their effects are well studied. Davies (1990) has given an excellent treatment of ionospheric propagation and reviews of particular relevance are given in (Evans, 1968) and (Hagfors, 1976).

#### The irregular effects :

The irregularities in the ionosphere perturb the cosmic signal. The predominant scale sizes in the ionization irregularities are found to be a few kilometres or less.

The effects of these fluctuations have been studied extensively at frequencies between 20 and 200 MHz. Hewish (1952), Booker (1958) and Lawrence, Little and Chivers (1964) have reviewed the early results and techniques. A comprehensive review of theory and observations of ionospheric fluctuations can be found in (Crane, 1977), (Fejer and Kelley, 1980) and (Yeh and Liu, 1982) and a summary of global morphology can be found in (Aarons, 1982).

The most important effect of ionospheric irregularities, is a random fluctuation in phase and amplitude known as phase scintillation and amplitude scintillation respectively. Spoelstra & Kelder (1982) have studied the effects of ionospheric

scintillation on synthesis telescopes. Due to change in phase of the measured visibility function, the image can be distorted as the phase carries the information about the spacing of the point sources in the image.

#### 1.4 SUMMARY OF PRESENT WORK

In this thesis a new approach to study the effects of ionospheric scintillation on the reconstructed image has been tried, with particular emphasis on GMRT. The present work tries to integrate the studies made by astronomers and the ionospheric propagation community. The common element and the starting point is the Mutual Coherence function or the Spatial Coherence function of Fomalont (1978). A lot of studies have been carried out on the effect of ionosphere on the mutual coherence function with the most recent and relevant one being that done by Bhattacharya & Rastogi (1991). Although they have carried out studies for single telescopes, the results are of a more fundamental nature and have been extended to spaced receivers, working as interferometric pairs.

The thesis is organised into five chapters. The second chapter describes the process of image reconstruction from visibility measurements and chapter 3 gives the details of ionospheric scintillation and its effect on the Mutual Coherence function. Chapter 4 discusses the details of the computer code generated for the work and chapter 5 discusses the results.

## CHAPTER - 2

### INTERFEROMETRY AND RADIO IMAGE MAPPING

#### 2.1 INTERFEROMETRY THEORY

The theory of aperture synthesis has been well summarised by Thomson, Moran and Swenson (1986). A simple interferometric arrangement is shown in Fig. 2.1.

For a point source, each antenna delivers the same signal voltage  $V$  with a phase difference determined by the baseline  $D$  and the source direction  $\theta$ . The integrator has a time constant  $2T$ . The output of the integrator resulting from a point source is

$$r(\tau) = \frac{1}{2T} \int_{-T}^T V(t) V(t - \tau) dt \quad (2.1)$$

The integration time  $2T$  is chosen to be very large as compared to  $\Delta\nu^{-1}$ , where  $\Delta\nu$  is the finite bandwidth of the two pre-detection amplifiers. Clearly the eqn. (2.1) is an autocorrelation function.

The time delay between the outputs of the two antennas is given by  $\tau_g = (D/C) \sin\theta$ .  $\tau_g$  is called the geometrical delay and  $C$  is the velocity of light. If  $V(t)$  has a sinusoidal variation of the form  $V(t) = \sin 2\pi\nu t$ . The output of the multiplier then is proportional to



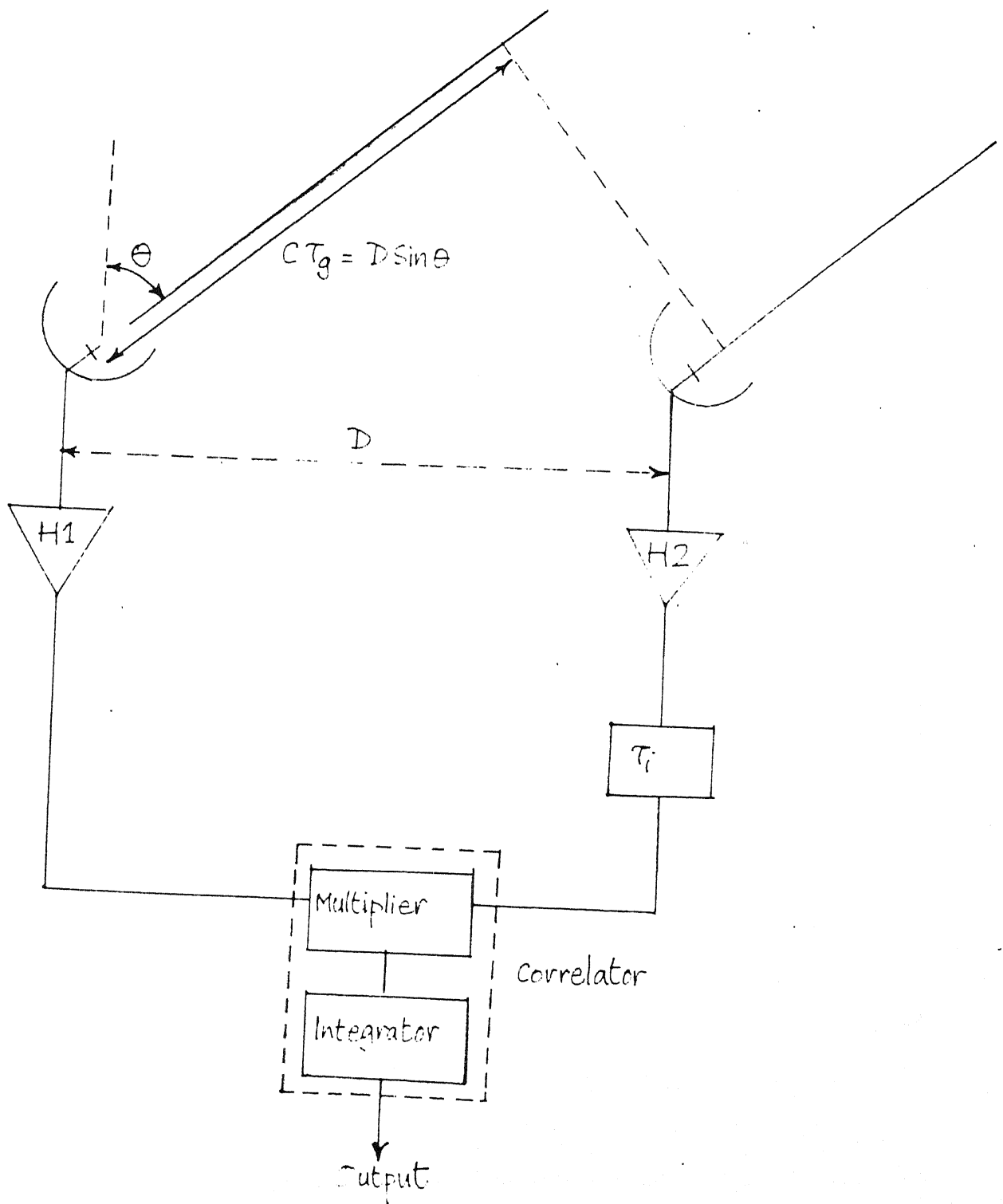


Fig. 2.1 : Elementary interferometer showing bandpass amplifiers  $H_1$  &  $H_2$ , geometrical time delay  $\tau_g$ , instrumental time delay  $\tau_i$ , and the correlator consisting of a multiplier and integrator.

$$F = 2\sin(2\pi\nu t) \sin 2\pi\nu(t-\tau_g) = \cos 2\pi\nu\tau_g - \cos(4\pi\nu t) \cos(2\pi\nu\tau_g) \\ - \sin(4\pi\nu t) \sin(2\pi\nu\tau_g) .$$

By filtering the more rapidly varying terms in  $F$  can be filtered out leaving

$$F = \cos \left[ \frac{2\pi D}{\lambda} \sin\theta \right] = \cos \left[ \frac{2\pi D\xi}{\lambda} \right]$$

where  $\xi = \sin\theta$  is the direction cosine measured with respect to the baseline.

The power spectrum of a signal is the Fourier transform of the autocorrelation function of the signal. This is known as the Wiener-Khinchin relation. This can be written mathematically as

$$\int_{-\infty}^{\infty} r(\tau) e^{-j2\pi\nu\tau} d\tau = |H(\nu)|^2 \quad (2.2a)$$

and

$$\int_{-\infty}^{\infty} |H(\nu)|^2 e^{j2\pi\nu\tau} d\nu = r(\tau) \quad (2.2b)$$

where  $H(\nu)$  is the amplitude (voltage) response, and hence  $|H(\nu)|^2$  is the power spectrum of the signal input to the multiplier. If we consider the cosmic signal to have a constant amplitude spectrum (which is valid almost universally), the amplitude spectrum  $H(\nu)$  is determined solely by the passband characteristics (frequency response) of the amplifiers. Thus the output of the interferometer as a function of the time delay  $\tau$  is

the Fourier transform of the power spectrum of the cosmic signal as bandlimited by the amplifiers.

If  $V(t)$  has a sinusoidal variation of the form  $\sin(2\pi\nu t)$ , then the output of the multiplier and the integrator comes out to be of the form

$$r(\tau) = \cos\left[\frac{2\pi D \xi \nu_o}{C}\right] \times \text{Bandwidth pattern.}$$

where  $\xi = \sin\theta$  is the direction cosine measured w.r.t. the baseline

$\nu_o$  = Center frequency of the band limited amplifier, and Bandwidth pattern depends upon the form of  $|H(\nu)|^2$ . For a uniform power spectral density, the bandwidth pattern =  $\frac{\sin(\pi D \xi \Delta\nu/C)}{\pi D \xi \Delta\nu/C}$  so that the correlation response is given by

$$r(\tau) = \cos\left[\frac{2\pi\nu_o D}{C} \sin\theta\right] \frac{\sin(\pi D \xi \Delta\nu/C)}{\pi D \xi \Delta\nu/C}$$

Figure 2.2 shows the point source response of the type given by the above equation.

In mapping applications, observations are made in the vicinity of the bandwidth pattern maxima and this condition is achieved by changing the instrumental delay  $\tau_i$  periodically so as to keep  $\tau = \tau_g - \tau_i$  suitably small.

The instrumental delay is calculated for a nominal source position  $\theta_o$  which becomes the reference position. Consider the

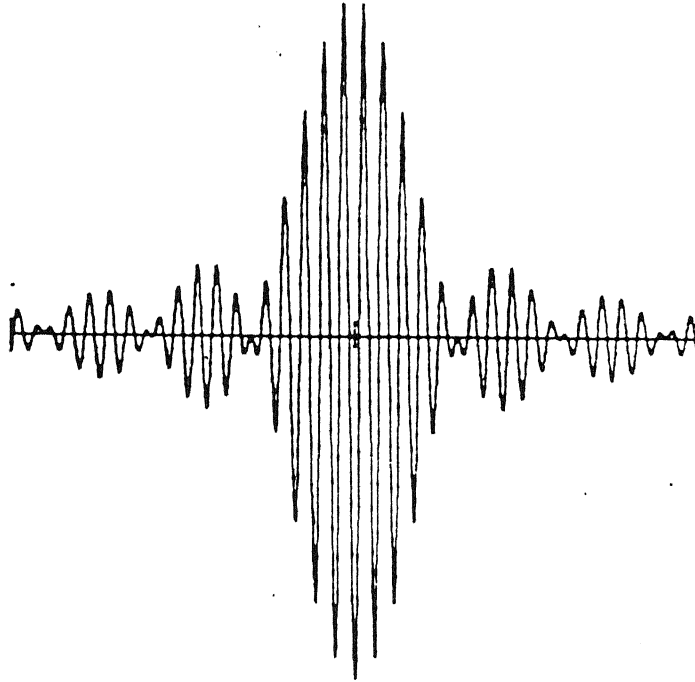


Fig. 2.2 : The point source response of an interferometer with rectangular passband. The abscissa is the geometrical delay  $\tau_g$ . The bandwidth pattern determines the envelope of the sinusoidal fringe term.

response to a narrow source at position P in the vicinity of  $\theta_0$ . Let  $\theta = \theta_0 - \theta'$  where  $\theta'$  is very small. Then, interferometer response is given by

$$F(\xi') = \cos(2\pi u \xi')$$

where  $\xi' = \sin\theta \approx \theta'$  is the direction cosine,  $u = \left[ \frac{\nu_0 D}{C} \right] \cos\theta_0 = \left[ D/\lambda_0 \right] \cos\theta_0$  is a spatial frequency term which is measured in cycles per radian, since the spatial variable  $\xi'$  being small, can be measured in radians.

## 2.2 SOURCE SYNTHESIS

If  $B_1(\xi')$  is the brightness of the source, we obtain the interferometric output as a function of  $\xi'$ .

$$R(\xi') = \Delta\nu \int_{\text{source}} \cos[2\pi u (\xi' - \xi'')] A(\xi'' - \xi') B_1(\xi'') d\xi''$$

where  $A(\xi')$  is the antenna response variation with direction.

Now for a particular value  $u = u_0$ , the Fourier transform of the fringe term  $\cos(2\pi u_0 \xi')$  is given by

$$\cos(2\pi u_0 \xi') = \frac{1}{2} [\delta(u - u_0) + \delta(u + u_0)]$$

Defining

$$b_1(u) \leftrightarrow B_1(\xi') \quad \text{and} \quad r(u) \leftrightarrow R(\xi')$$

and assuming broad enough antenna beams so that gain is constant over the source we have

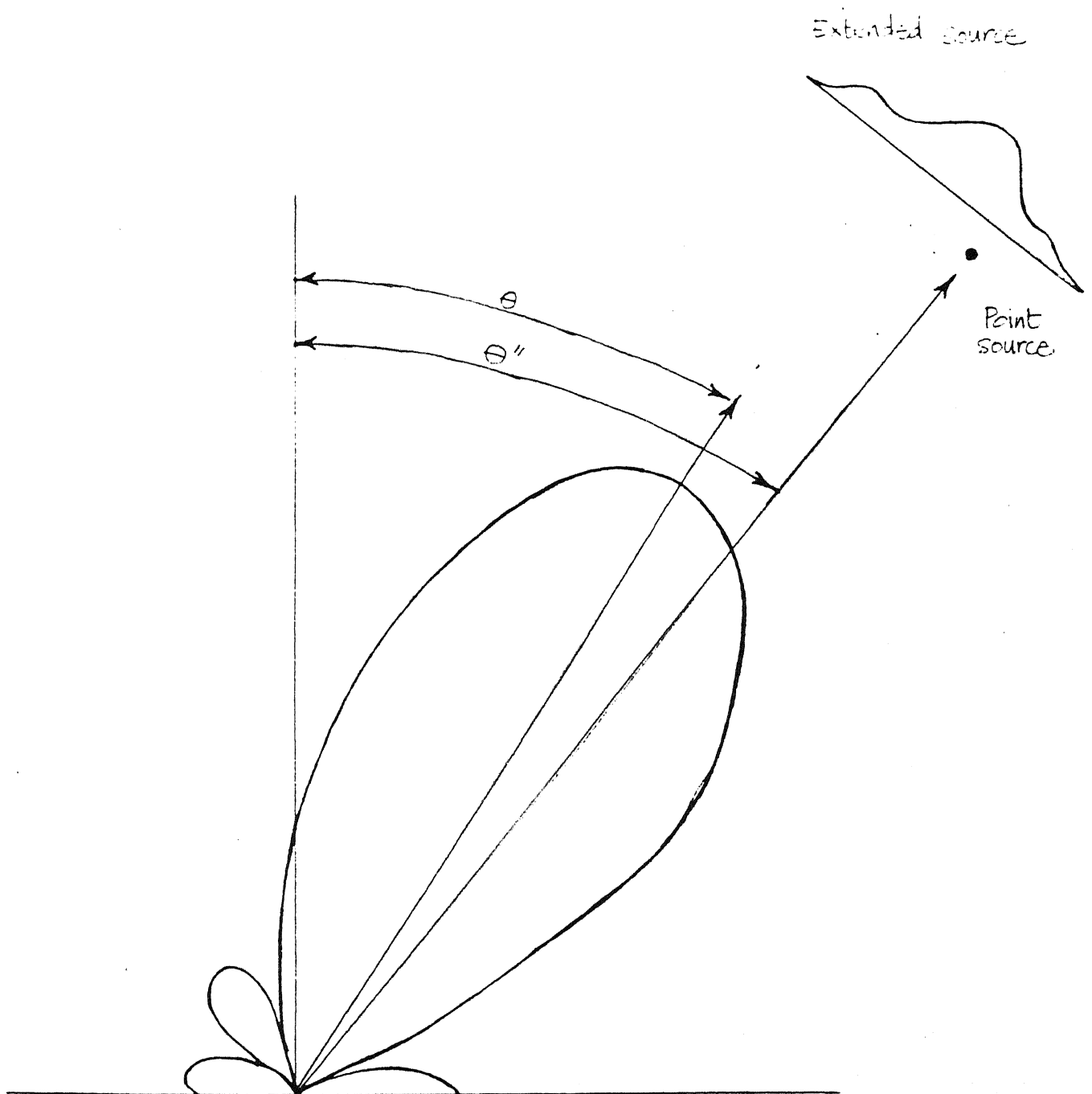


Fig. 2.3 : Power reception pattern of a typical antenna, which is a polar plot of effective area versus angle of arrival of plane-wave radiation.

$$r(u) = \frac{1}{2} A \Delta \nu \left[ b_1(u_0) \delta(u-u_0) + b_1(-u_0) \delta(u+u_0) \right]$$

Hence  $r(u)$  constitutes the angular (spatial) frequency spectrum of the source brightness function as filtered by the interferometer, which passes only the spatial frequencies  $\pm u_0$ .

Consider an interferometer with an east-west baseline and an extended cosmic source that passes through the interferometer reception pattern from east to west as the earth rotates. Each hour angle of the source corresponds to a different value of the angle between the baseline and the direction to the source, and thus to a different spatial frequency  $u$ . The variable  $\xi'$  also increases with time, so the output of the interferometer varies cosinusoidally (or sinusoidally) with time over small intervals. The earlier equation shows that at any instant the amplitude of the fringe pattern from the correlator  $r(\xi)$  is equal to the even part of the Fourier transform of  $B_1(\xi')$ , that is, to the cosine transform of the brightness with respect to the point on the source at position angle  $\theta_0$  at that time. With respect to this same point on the source at an instant one-quarter of a fringe cycle later in time the output fringe pattern is equal to the sine transform, which is the imaginary part of the brightness Fourier transform. Thus the output fringe pattern contains both the real and imaginary parts of  $b_1(u)$ , the Fourier transform  $B_1(\xi')$ . In practice, a phase reference position on the sky is designated, central to the region of the interest, and the fringe pattern is then computed for a hypothetical point source of unit

flux density at this position. The amplitude and phase of the observed fringe pattern are measured with respect to the hypothetical fringes. The resulting values, when expressed as a complex quantity, are known as the complex visibility  $V(u)$ , which is equal to  $b_1(u)$ . The complex visibility, as derived from the measured output of an interferometer, includes the effects of the antenna beams, the finite receiving bandwidth and any instrumental imperfections in addition to the effects of the atmosphere. In practice the antennas often track the source, so  $B_1$  is multiplied by  $A_1$ . Then

$$R(\xi') = \Delta\nu \int_{\text{source}} \cos \left[ 2\pi u (\xi' - \xi'') \right] A(\xi'') B_1(\xi'') d\xi''$$

If the phases and amplitudes of the fringes are observed at frequent enough intervals in  $u$ , the complex spatial spectrum represented by  $V(u)$  is obtained. Then by Fourier transforming this spectrum and correcting for  $A_1$  the source brightness distribution can be reconstructed.

While observations of a source for many hours with a single baseline can yield, in principle, a wide range of spatial frequencies, in practice they usually cannot produce a complete enough spectrum to permit satisfactory reconstruction of a source profile. Several different baseline are thus required. These may be obtained from  $n_a(n_a-1)/2$  pairs in a set of  $n_a$  antennas that form an array.



### 2.3 TWO DIMENSIONAL MAPPING

In the particular case of an east-west baseline and an equatorial source, the source can be mapped in the east-west dimension only, as the spatial frequency spectrum so derived has only one frequency dimension,  $u$ . To synthesize a map in two dimensions requires a two dimensional spatial frequency spectrum in the  $(u,v)$  frequency domain,  $v$  being the north-south frequency component. This may be accomplished for an equatorial source by observing with a two-dimensional array of interferometers. The two-dimensional situation is similar to the one-dimensional one but more complicated. It can be understood by using the more general form of the visibility function which is given as

$$V\left[\bar{D}_\lambda\right] = \int_{4\pi} A_N(\bar{\sigma}) B(\bar{\sigma}) e^{-j2\pi\bar{D}_\lambda \cdot \bar{\sigma}} d\Omega.$$

where  $V \rightarrow$  complex fringe visibility

$\bar{D}_\lambda \rightarrow$  baseline vector of the two antennas

$A_N(\bar{\sigma}) \rightarrow$  is the normalized antenna area

$B(\bar{\sigma}) \rightarrow$  is the radio brightness

$d\Omega \rightarrow$  an element of solid angle on the sky  $\bar{\sigma} = \bar{S} - \bar{S}_0$  as shown in Fig. 2.4.

$(\xi, \eta, \zeta)$  are the direction cosines of  $\hat{s}$ .  $\hat{S}_0$  is the reference direction and its direction cosines are  $(0,0,1)$ .

Since

$$\bar{D}_\lambda \cdot \hat{S} = u\xi + v\eta + w\zeta$$

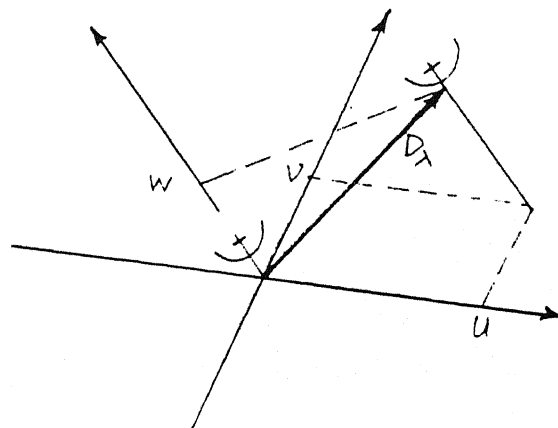
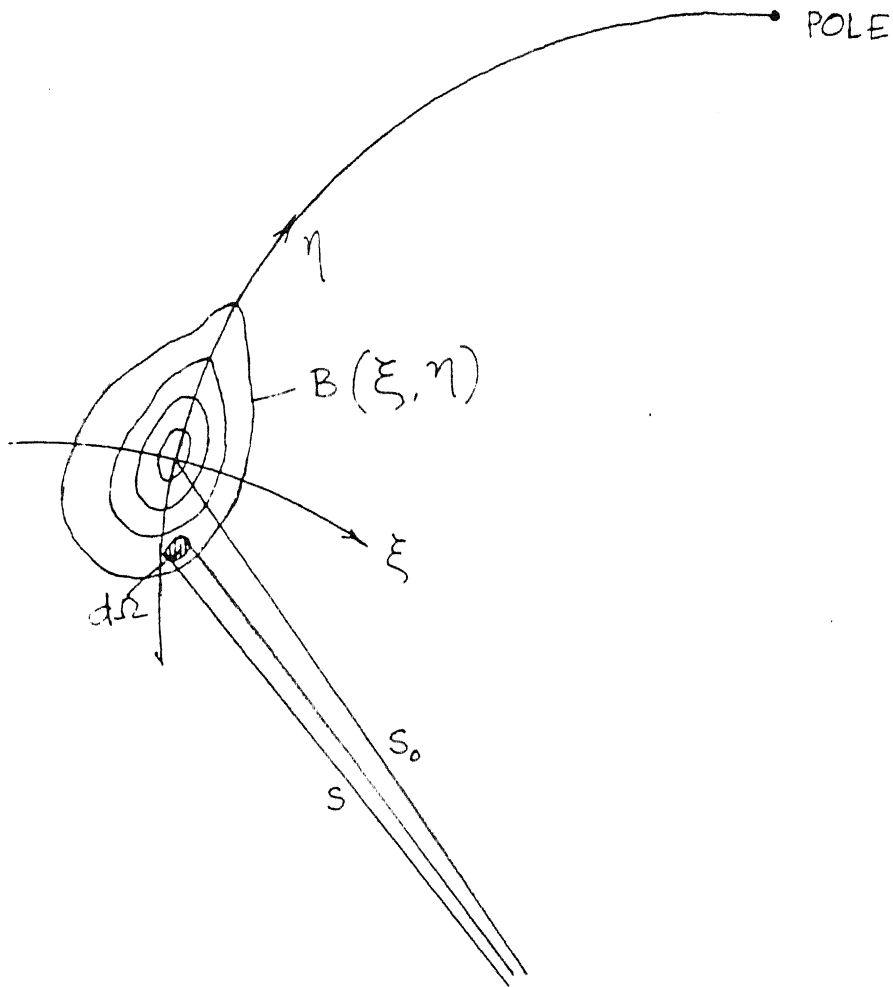


Fig. 2.4 : Geometrical relationship between a source under observation  $B(\xi, \eta)$  and an interferometer or one antenna pair of an array. The spacing vector  $\bar{D}_\lambda$  of the antennas has components  $(u, v, w)$ .

For small source

$$\bar{\sigma} = \hat{S} - \hat{S}_0 \text{ is small}$$

Since

$$\xi, \eta \text{ are small and } \zeta \simeq 1.$$

Under these conditions we have

$$d\Omega = \frac{d\xi d\eta}{\sqrt{1 - \xi^2 - \eta^2}} \simeq d\xi d\eta$$

and we have

$$V(u, v, w) = \int_{-\infty}^{\infty} \int_{-\infty}^{\infty} A_N(\xi, \eta) B(\xi, \eta) \times \exp \left\{ -j2\pi \left[ u\xi + v\eta + w(\zeta - 1) \right] \right\} \frac{d\xi d\eta}{\sqrt{1 - \xi^2 - \eta^2}}$$

which reduces to

$$V(u, v, w) = V(u, v, 0) = \int_{-\infty}^{\infty} \int_{-\infty}^{\infty} A_N(\xi, \eta) B(\xi, \eta) e^{-j2\pi(u\xi + v\eta)} d\xi d\eta$$

#### 2.4 ANTENNA SPACING COORDINATES AND (u, v) LOCII

A right handed Cartesian coordinate system in which X and Y are measured in plane parallel to the earth's equator, X in the meridian plane (defined as the plane through the poles of the earth and the reference point in the array), Y towards the east, and Z is measured toward the north pole. If  $(X_\lambda, Y_\lambda, Z_\lambda)$  are the components of  $\bar{D}_\lambda$  in the (X, Y, Z) system, the components (u, v, w) are given by

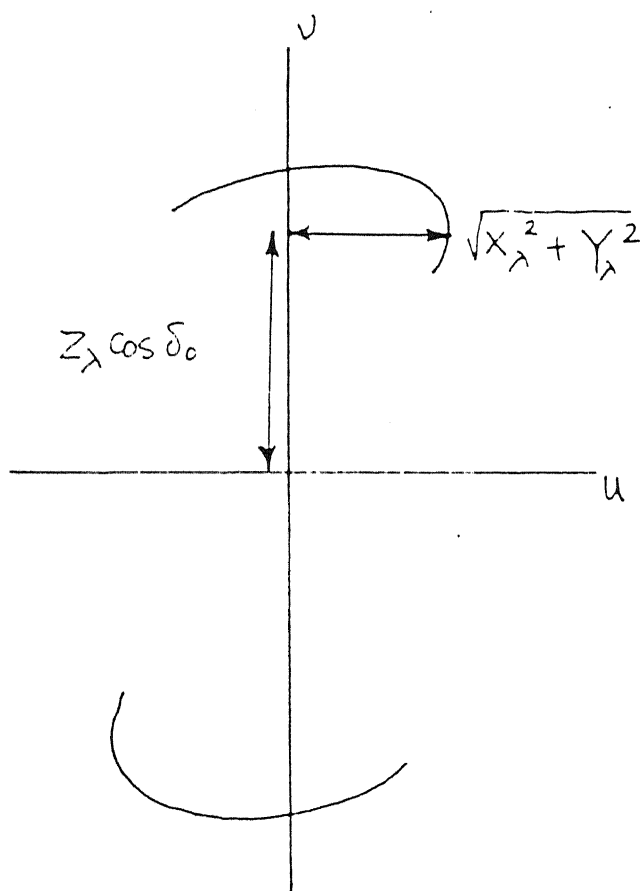


Fig. 2.5 : Spacing vector locus in the  $(u, v)$  plane. The lower arc in the diagram represents the locus of conjugate values of visibility. Unless the source is circumpolar the cutoff at the horizon limits the lengths of the arcs. horizon limits the lengths of the arcs

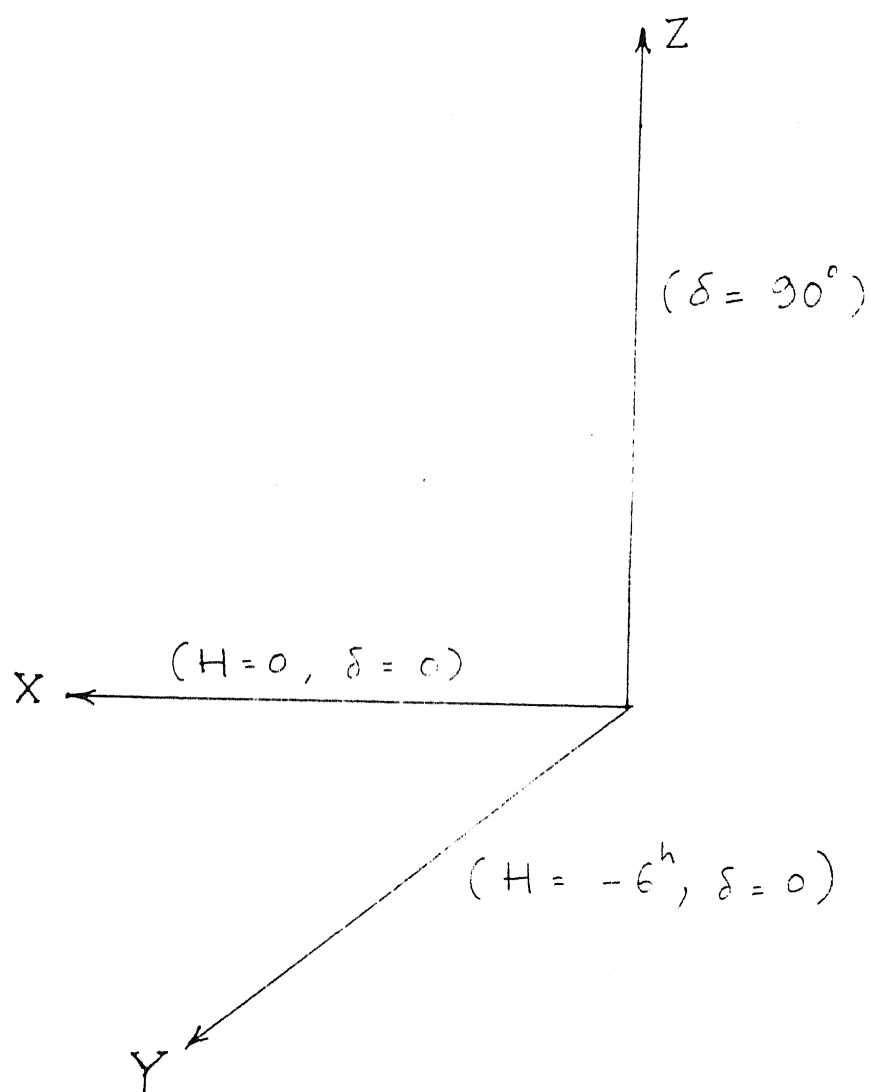


Fig. 2.6 : The coordinate system for the baseline measurement

$$\begin{bmatrix} u \\ v \\ w \end{bmatrix} = \begin{bmatrix} \sin H & \cos H & 0 \\ -\sin \delta \cos H & \sin \delta \sin H & \cos \delta \\ \cos \delta \cos H & -\cos \delta \sin H & \sin \delta \end{bmatrix} \begin{bmatrix} X_\lambda \\ Y_\lambda \\ Z_\lambda \end{bmatrix}$$

where  $(H, \delta)$  are the hour angle and the declination of the phase reference position. Examination of above equations shows that

$$u^2 + \left[ \frac{v - Z_\lambda \cos \delta_o}{\sin \delta_o} \right]^2 = X_\lambda^2 + Y_\lambda^2.$$

which defines an ellipse in the  $(u, v)$  plane with hour angle as the variable. The ellipse is centred on the  $v$  axis at  $(u, v) = (0, Z_\lambda \cos \delta_o)$  with semimajor and semiminor axes equal to  $\sqrt{X_\lambda^2 + Y_\lambda^2}$  and  $\sin \delta_o \sqrt{X_\lambda^2 + Y_\lambda^2}$ . Since  $V(-u, -v) = V^*(u, v)$ , any observation supplies simultaneous measurements on two arcs, which are part of the same ellipse only if  $Z_\lambda = 0$ . Fig. 2.6 describes the co-ordinate system used.

## 2.5 DISCRETE FOURIER TRANSFORMATION

The discrete transform is very widely used in synthesis mapping because of computational advantages. With the discrete transform the function  $V(u, v)$  and  $B(\xi, \eta)$  are expressed as rectangular matrices of sampled values at uniform increments in the two variables involved. The main advantage of this system is that the Fast Fourier transform (FFT) algorithm can be used to reduce the computation time. The two-dimensional form of the discrete transform for a fourier pair  $f$  and  $g$  is defined by

$$f(m,n) = \frac{1}{MN} \sum_{k=0}^{M-1} \sum_{l=0}^{N-1} g(k,l) e^{-j2\pi km/M} e^{-j2\pi ln/N}$$

and the inverse is

$$g(k,l) = \sum_{m=0}^{M-1} \sum_{n=0}^{N-1} f(m,n) e^{j2\pi km/M} e^{j2\pi ln/N}$$

To apply the discrete transform to the synthesis-mapping problem we first use an interpolation to obtain values of  $V(u,v)$  at points separated by  $\Delta u$  in  $u$  and  $\Delta v$  in  $v$  as shown in Fig. 2.7.

The dimensions of the  $(u,v)$  plane that contain these data are  $M\Delta u$  by  $N\Delta v$ . In the  $(\xi, \eta)$  plane the points are spaced  $\Delta \xi$  in  $\xi$  and  $\Delta \eta$  in  $\eta$  and the map dimensions are  $M\Delta \xi$  by  $N\Delta \eta$ . The dimensions in the two domains are related by

$$\Delta u = \left[ M \Delta \xi \right]^{-1}$$

$$\Delta v = \left[ N \Delta \xi \right]^{-1}$$

$$\Delta \xi = \left[ M \Delta u \right]^{-1}$$

$$\Delta \eta = \left[ N \Delta v \right]^{-1}$$

The transformation between  $V(u,v)$  and  $B(\xi,\eta)$  is obtained by substituting  $g(k,l) = B(k\Delta \xi, l\Delta \eta)$  and  $f(m,n) = V(m\Delta u, n\Delta v)$ , so that

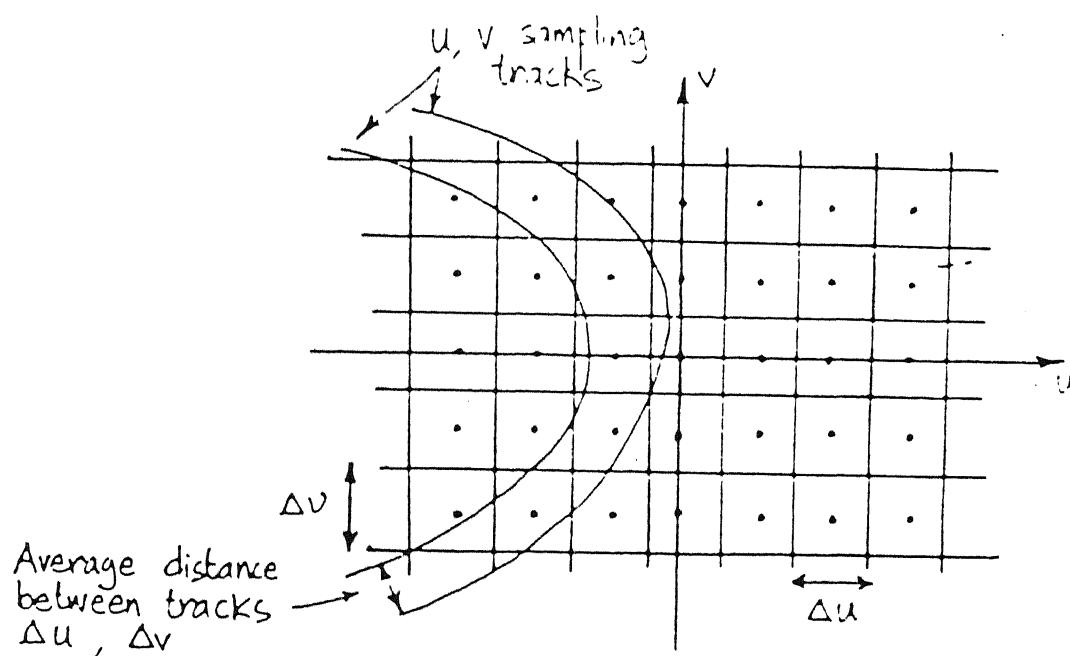


Fig. 2.7 : Points on a rectangular grid in the  $(u, v)$  plane at which the visibility is sampled for use with the discrete Fourier transform. As shown, the spacings  $\Delta u$  and  $\Delta v$  are equal. The division of the plane into cells for interpolation using the cell-averaging technique is also shown.



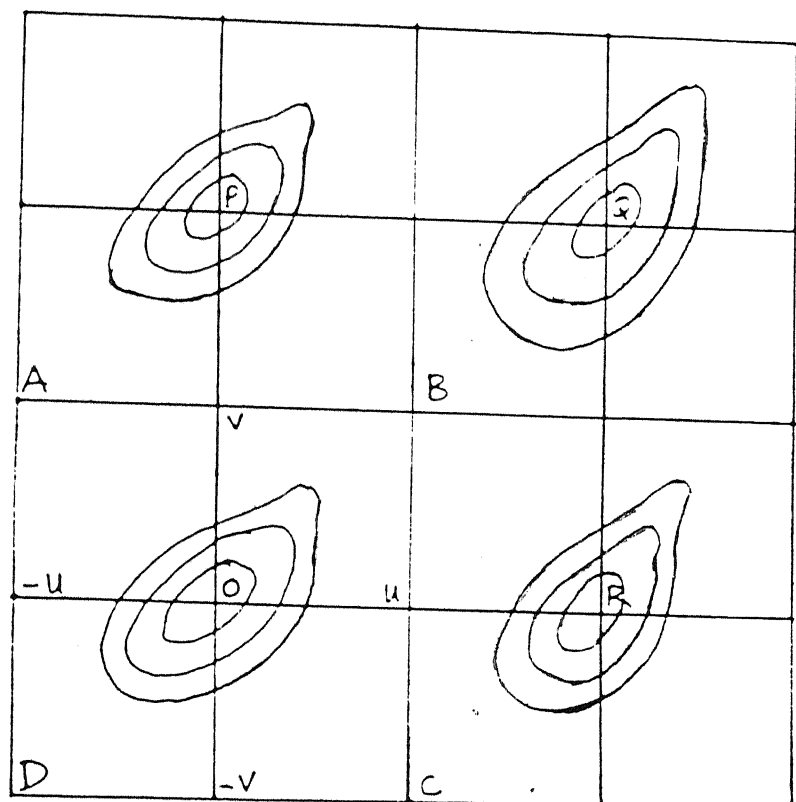


Fig. 2.8 : Rearrangement of a visibility function for input to the discrete Fourier transform. The  $(u,v)$  origin is at 0. The contours represent the unsampled visibility which is measured in the range of  $u$  and  $v$  within the area ABCD. In the transformation of the sampled data the function is, in effect, replicated at points such as P, Q, and R. The input and output to the transformation process cover only the positive values of  $u$  and  $v$  and are represented by the area OPQR.

$$V(m\Delta u, n\Delta v) = \sum_{k=-\infty}^{\infty} \sum_{l=-\infty}^{\infty} B(k\Delta\xi, l\Delta\eta) e^{-j2\pi(km\Delta u\Delta\xi + ln\Delta v\Delta\eta)} \Delta\xi\Delta\eta$$

and

$$B(k\Delta\xi, l\Delta\eta) = \sum_{m=-\infty}^{\infty} \sum_{n=-\infty}^{\infty} V(m\Delta u, n\Delta v) e^{j2\pi(km\Delta u\Delta\xi + ln\Delta v\Delta\eta)} \Delta u\Delta v$$

The Fourier transform relationship between the sampled functions requires that they be regarded as periodic, with periods  $M\Delta u$  and  $N\Delta v$  in  $u$  and  $v$  and  $M\Delta\xi$  and  $N\Delta\eta$  in  $\xi$  and  $\eta$ . This is illustrated in Fig. 2.8.

A very important problem that has to be addressed is the problem of obtaining values of  $V(u,v)$  at the required points in the  $(u,v)$  plane. These points form a rectangular grid, as shown in Fig. 2.7, while the measured visibility values lie on the elliptical spacing locii. A very simple means of obtaining values at the grid points is to divide the  $(u,v)$  plane into rectangular cells of dimensions  $\Delta u$  by  $\Delta v$  centred on the grid points as shown in Fig. 2.7. The mean of all measured points within each cell is then computed and assigned to the grid point at the cell center. Grid points for which there are no measurements within the cell are assigned a value of zero. This procedure has been termed cell averaging. A 15 dB gaussian taper is applied to the visibility data in the grid. This reduces the aliasing of false details from outside the region for which the mapping is being done.

## 2.6 MUTUAL COHERENCE FUNCTION

The generalised mutual coherence function is the measure of correlation in a radiation field between two points  $\bar{r}_1$  and  $\bar{r}_2$  at a time difference  $\tau$  and is defined as

$$\Gamma(\bar{r}_1, \bar{r}_2, \tau) = \langle S(\bar{r}_1, t) S^*(\bar{r}_2, t+\tau) \rangle$$

where  $S(\bar{r}, t)$  is the response of the probe which is proportional to the radiation field  $E(\bar{r}, t)$  at any point in space  $\bar{r}$  at any time  $t$ . For the special case of  $\tau=0$

$$\Gamma(\bar{r}_1, \bar{r}_2, 0) = \Gamma(\bar{r}_1, \bar{r}_2) = \langle S(\bar{r}_1, t) S^*(\bar{r}_2, t) \rangle$$

is known as the spatial coherence function of the field. This coherence function when measured with the limitations of the finite bandwidth and beamwidth of the amplifiers and the antenna is known as the Visibility function, defined earlier. As has been mentioned earlier the relationship between the spatial coherence function and the brightness distribution is given by the Van Citterte Zernicke theorem, a simplified version of which is

$$\Gamma(u, v) \leftrightarrow B(\xi, \eta)$$

If  $\hat{\Gamma}$  be the discretized and sampled MCF and  $\hat{\Gamma}_m$  be the discretized and sampled MCF with the effect of the ionosphere then we can define the following Fourier relationship

$$\hat{\Gamma}(u, v) W(u, v) \leftrightarrow \hat{B}(\xi, \eta)$$

and  $\hat{\Gamma}_m(u, v) W(u, v) \leftrightarrow \hat{B}_m(\xi, \eta)$

where  $W(u,v)$  is the sampling function which depends upon the grid points sampled in the  $(u-v)$  plane as explained earlier.

Also

$$\hat{\Gamma}_m(u_1, v_1) = \hat{\Gamma}(u_1, v_1) I(u_1, v_1)$$

where  $I(u_1, v_1)$  defines the effect of the ionosphere on the measured spatial coherence function.

Henceforth in the thesis the terms visibility function and the spatial coherence function have been used interchangeably. The factor  $I(u,v)$  will be shown to depend upon the structure function of phase fluctuations in Chapter 4.

## CHAPTER - 3

### IONOSPHERIC SCINTILLATION AND MUTUAL COHERENCE FUNCTION

As described in Chapter 1, the variation in the amplitude and phase of the signal is known as scintillation of amplitude and phase respectively. Most of what follows in the next 3 sections is based upon the analysis presented in (Yeh and Liu, 1982), (Ishimaru, 1978) and (Tatarskii, 1971).

#### 3.1 IONOSPHERIC IRREGULARITIES AND THEIR CHARACTERIZATION

As has been noted earlier in Chapter 1, the permittivity of the ionosphere is given as

$$\epsilon = 1 - \frac{N_e e^2}{4\pi^2 \nu^2 \epsilon_0 m}$$

where  $N_e \rightarrow$  electron concentration

$e \rightarrow$  charge on an electron

and  $m \rightarrow$  mass of the electron.

Due to random variations in the density of electron in the ionosphere, the emerging wavefront experiences a change of optical phase given by

$$\Delta\phi = \int \Delta n \, dl$$

path through  
ionosphere

where  $\Delta n$  is the refractive index fluctuation caused by electron density fluctuations  $\Delta n$ . This change in the wavefront phase is

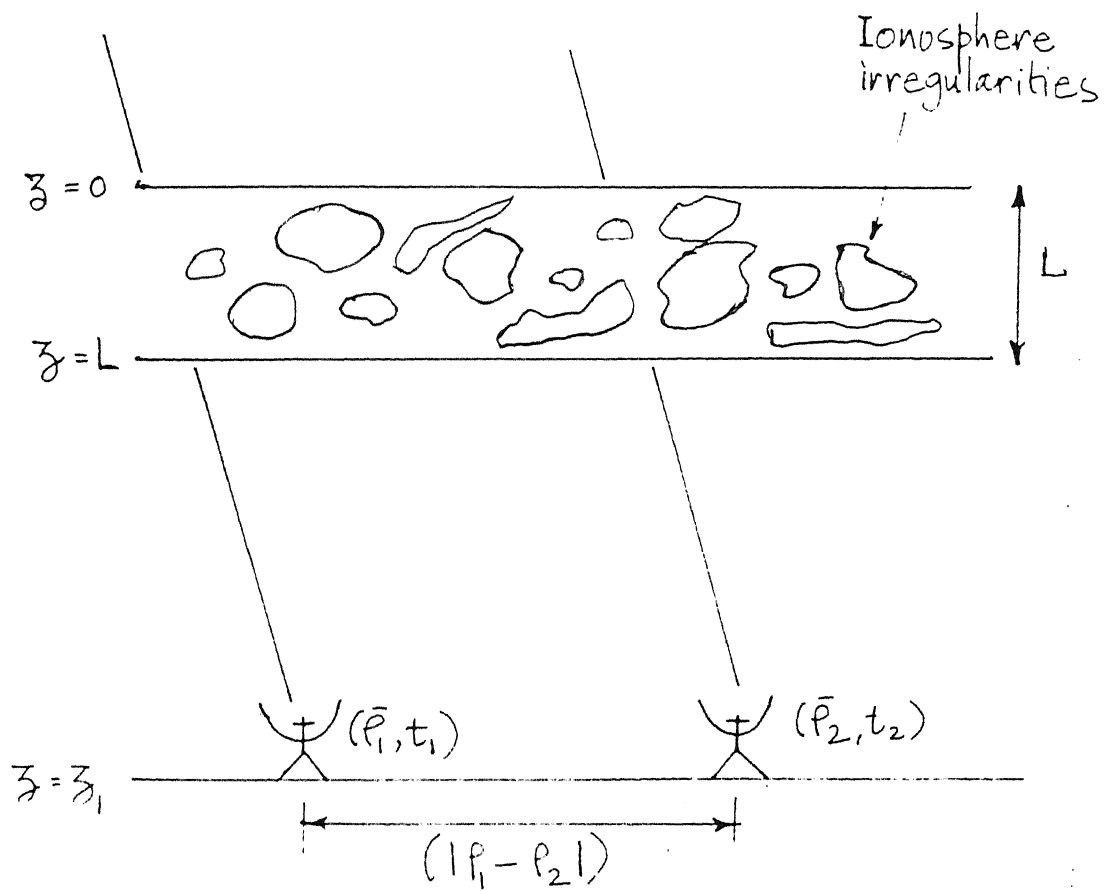


Fig.3.1 : The geometry of the problem : The thin phase screen approximation. The position vector of a point is defined as  $\bar{r} = x\hat{i}_x + y\hat{i}_y + z\hat{i}_z = \bar{\rho} + z\hat{i}_z$

what causes scintillation, both phase and amplitude. To study further the effects of the ionosphere we consider the thin screen model of ionospheric irregularities. In this model, the irregularities are confined to a screen extending from  $z=0$  to  $z=L$ . The geometry is given in Fig. 3.1. Now we shall define some quantities of interest to be used later.

### 1. Correlation function and spectra

If  $\Delta N(\vec{r})$  is the fluctuation of electron density from the background  $N_0$ , then if  $\Delta N(\vec{r})$  is assumed to be a homogeneous random field with a zero mean, then its correlation function is  $B_{\Delta N}(\vec{r}_1 - \vec{r}_2) = \langle \Delta N(\vec{r}_1) \Delta N(\vec{r}_2) \rangle$ , where the angular brackets denote the process of ensemble averaging. By the Wiener-Khinchin theorem, the correlation and the spectrum form a Fourier transform pair.

$$\Phi_{\Delta N}(\vec{K}) = (2\pi)^{-3} \iiint_{-\infty}^{\infty} B_{\Delta N}(\vec{r}) e^{-j\vec{K} \cdot \vec{r}} d^3r$$

$$B_{\Delta N}(\vec{r}) = \iiint_{-\infty}^{\infty} \Phi_{\Delta N}(\vec{K}) e^{j\vec{K} \cdot \vec{r}} d^3K$$

If the irregularities are isotropic, the correlation function depends only on  $|\vec{r}_1 - \vec{r}_2|$ . In-situ measurements and scintillation studies have revealed a variation of the form

$$\Phi_{\Delta N}(K) \propto K^{-p}$$

where isotropicity of irregularities is assumed.

The values of  $p$  have been found to be close to 4. However, in reality it has been found that the irregularities are anisotropic and aligned along the earth's magnetic field. In the work of Rino and Fremouw (1977) it is shown that for a fairly general anisotropic model

$$\Phi_{\Delta N}(\bar{q}) = ab \langle \Delta N^2 \rangle \cdot Q(q)$$

$$\text{where } q^2 = AK_x^2 + BK_x K_y + CK_y^2$$

The parameters  $a$  and  $b$  are axial ratios along and transverse to the principal irregularity axis, respectively.

The function  $Q(q)$  gives the shape of the spectral density function (SDF). It is normalized to unit area. Thus for a power law SDF, the appropriate functional form is

$$Q(q) = \frac{8\pi^{3/2} \Gamma(\nu+1/2) / \Gamma(\nu-1) q_o^{2\nu-2}}{\left[ q_o^2 + q^2 \right]^{\nu+1/2}}$$

where  $q_o$  is the outer-scale cut-off wave number. The coefficients  $A$ ,  $B$  and  $C$  depend on the propagation angles relative to the principle irregularity axis, and  $\Gamma(\nu)$  is the gamma function.

The form of SDF is given in Fig. 3.2. By making the definition

$$C_s = 8\pi^{3/2} \langle \Delta N^2 \rangle q_o^{2\nu-2} \Gamma(\nu+1/2) / \Gamma(\nu-1)$$

it follows that

$$\Phi_{\Delta N}(q) = \frac{abC_s}{(q_o^2 + q^2)^{\nu+1/2}}$$



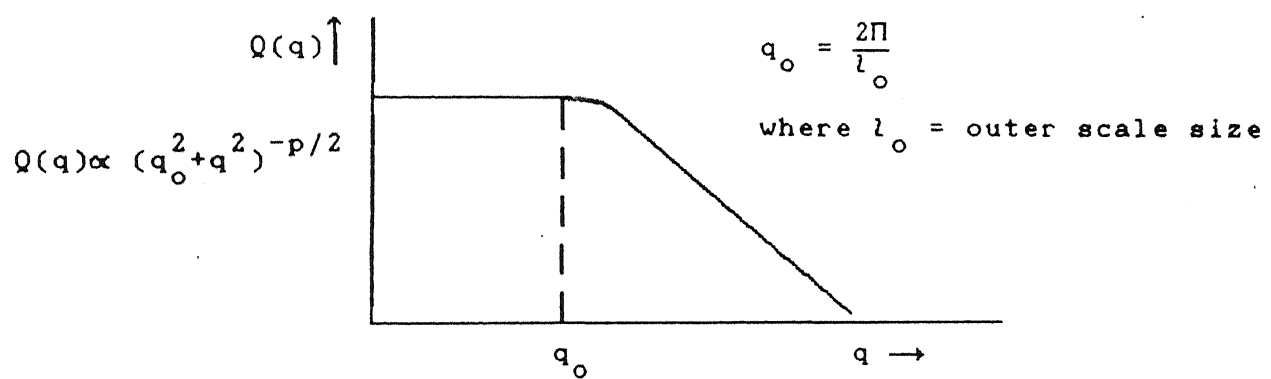


Fig. 3.2 : The spectral density function  $Q(q)$

### 3.2 OPTICAL PATH STRUCTURE FUNCTION

At times the electron density fluctuations and hence the optical path fluctuation as defined by

$$\delta\phi(\bar{\rho}) = \int \Delta n(\bar{\rho}, z) dz$$

where  $\bar{\rho} = (x, y)$  is the transverse co-ordinate and  $\Delta n$  is the refractive index fluctuations caused by electron density fluctuations.

There is a background trend as they are not strictly homogenous but only locally homogenous. In these cases it is more convenient to deal with the structure function  $D$  defined by

$$D_{\Delta n}(\bar{r}) = \langle [\Delta n(\bar{r} + \bar{r}') - \Delta n(\bar{r}')]^2 \rangle$$

The structure function for the optical path  $D_{\Delta\phi}(\bar{\rho})$  is just the mean square value of the optical path difference between two points separated by  $\bar{\rho}$  on the  $z = \text{constant}$  plane. This optical path structure function can be shown to be

$$\begin{aligned} D_{\phi}(\bar{\rho}) &= \langle [\delta\phi(\bar{\rho} + \bar{\rho}') - \delta\phi(\bar{\rho}')]^2 \rangle \\ &= 2 \left[ \langle \delta^2\phi(\bar{\rho}') \rangle - \langle \delta\phi(\bar{\rho}') \delta\phi(\bar{\rho} + \bar{\rho}') \rangle \right] \\ &= 2 \left[ R_{\delta\phi}(0) - R_{\delta\phi}(\bar{\rho}) \right] \end{aligned}$$

where  $R_{\delta\phi}(\bar{\rho}_1 - \bar{\rho}_2) = \langle \delta\phi(\bar{\rho}_1) \delta\phi(\bar{\rho}_2) \rangle$

The form  $R_{\delta\phi}$  has been given in (Rino, 1979) and the result is

$$R_{\delta\phi}(y) = r_e^2 \lambda^2 L \sec \theta G C_s \left| \frac{y}{2q_0} \right|^{\nu-1/2} \frac{K_{\nu-1/2}(q_0 y)}{2\pi\Gamma(\nu + \frac{1}{2})}$$

which gives

$$D_{\phi}(\Delta\bar{\rho}) = \frac{r_e^2 \lambda^2 (C_s L) \sec \theta G}{2\pi\Gamma(\nu + \frac{1}{2})} q_0^{1/2-\nu} \cdot \left[ \Gamma(\nu - \frac{1}{2}) q_0^{1/2-\nu} - 2K_{\nu-1/2}(q_0 y) \left( \frac{y}{2} \right)^{\nu-1/2} \right]$$

where

- $r_e$  → classical electron radius
- $\lambda$  → wavelength of incident radiation
- $C_s$  → strength of turbulence as defined earlier
- $q_0$  → spatial frequency corresponding to outer scale size
- $K_{\nu}(x)$  → modified bessel function of second kind and order  $\nu$
- $G$  → A geometrical factor

$$y = \left[ \frac{C \Delta \rho_{sx}^2 - B \Delta \rho_{sx} \rho_{sy} + A \Delta \rho_{sy}^2}{AC - \frac{B^2}{4}} \right]^{1/2}$$

where A, B and C are factors depending upon the angle of incidence and anisotropy and  $\delta\rho_{sx}$  and  $\Delta\rho_{sy}$  are quantities related to the differences in coordinates of the observing point,  $\bar{\Delta\rho}$ .

### 3.3 MCF AND THE STRUCTURE FUNCTION

In this section the relation between MCF and the structure function is explained. For this we consider the simplified case

of normal incidence. The geometry of propagation is the same as given in chapter 2.

In this case a component of the wave electric field is usually expressed as

$$E(\bar{r}, t) = u(\bar{r}, t) \exp \left[ -j (kz - \omega t) \right] \quad (3.1)$$

where  $u(\bar{r}, t)$  is the complex amplitude of the wave field and  $k$  and  $\omega$  are the wave number and the angular frequency of the wave. The time scale  $\tau_0$  for temporal variation of the irregularities is such that  $\omega \gg 2\pi/\tau_0$ . Hence under the forward scattering assumption the complex amplitude  $u$  still satisfies the parabolic equation

$$-2jk \frac{\partial u}{\partial z} + \nabla^2 u = -k^2 \epsilon_1(\bar{r}, t) u \quad (3.2)$$

where  $\epsilon_1$  represents the fluctuating part of the refractive index of the medium relative to the average refractive index.

It has been demonstrated (Lee, 1974) that the MCF,  $\Gamma$  satisfies the following equation

$$\begin{aligned} \frac{\partial \Gamma}{\partial z} = & - \left[ \frac{j}{2k} \right] \left[ \nabla_{\perp}^2 - \nabla_{\perp}'^2 \right] \Gamma \\ & - (4\pi r_e^2 / k^2) \left[ A_{\Delta N}(0, 0) - A_{\Delta N}(\bar{\rho} - \bar{\rho}', t - t') \right] \Gamma \end{aligned} \quad (3.3)$$

where  $r_e$  is the classical electron radius and  $A_{\Delta N}(\bar{\xi}, \tau)$  is the integrated space-time correlation function for the electron density fluctuations  $\Delta N(\bar{r}, t)$  :

$$A_{\Delta N}(\bar{\xi}, \tau) = \int_{-\infty}^{\infty} B_{\Delta N}(\bar{\xi}, z, \tau) dz \quad (3.4)$$

On making the co-ordinate transformation  $\bar{\xi} = \bar{\rho} - \bar{\rho}_1$ ,  $\bar{X} = (\bar{\rho} + \bar{\rho}')/2$  and using the fact that  $\Gamma$  must be independent of  $\bar{X}$  for a homogenous random medium, it is seen that  $\Gamma(\bar{\xi}, z)$  satisfies the equations

$$\begin{cases} \frac{\partial \Gamma}{\partial z} = -r_e^2 \lambda^2 \left[ A_{\Delta N}(0,0) - A_{\Delta N}(\bar{\xi}, \tau) \right] \Gamma ; & 0 \leq z \leq L \\ \text{and } \frac{\partial \Gamma}{\partial z} = 0 ; & z > L \end{cases} \quad (3.5)$$

For the spatial coherence function  $\tau=0$  and the solution for the above equations becomes

$$\Gamma(\Delta\bar{\rho}, z) = \Gamma(\Delta\bar{\rho}, 0) \exp \left\{ -r_e^2 \lambda^2 L \left[ A_{\Delta N}(0,0) - A_{\Delta N}(\Delta\bar{\rho}, 0) \right] \right\}$$

which can be rewritten as

$$\Gamma(\Delta\bar{\rho}, z) = \Gamma(\Delta\bar{\rho}, 0) \exp \left\{ -\frac{D_{\Delta\phi}(\bar{\Delta\rho})}{2} \right\} \quad (3.6)$$

or

$$\Gamma(u, v) = \Gamma^0(u, v) \exp \left\{ -\frac{D_{\Delta\phi}(\bar{\Delta\rho})}{2} \right\} \quad (3.7)$$

The term  $\exp \left\{ -\frac{D_{\Delta\phi}(\bar{\Delta\rho})}{2} \right\}$  defines the ionospheric contribution term  $I(u, v)$ . Even though the above relation has been derived for normal incidence, it is true for generalized oblique incidence also (Rino, 1978).

## CHAPTER - 4

### PROGRAM CODE DESCRIPTION

The aim of this work is to study the effects of the ionosphere on reconstructed radio-images. The program code can be separated into two distinct parts. In fact the first part makes use of the second.

The main program is the first and this part is responsible for

- i) Calculating the  $W(u,v)$  function
- ii) Generating the model gaussian sources
- iii) Calculating the various forward and inverse transforms,
- and iv) Calculating the maximum and r.m.s. dB errors between the assumed source image (A), the reconstructed image without the effect of ionosphere (B) and the reconstructed image with the effect of the ionosphere (C).

$W(u,v)$  function behaves as a spatial frequency filter. It arises due to the inherent limitations of the process of measurement of spatial frequencies by the synthesis telescope. This is introduced due to the finite size of the telescopic array. If we could somehow measure all the  $(u,v)$  frequency components then this would be a constant function. Since this is not so, we have a two-dimensional function with 'holes' in it corresponding to the unsampled frequency components. These

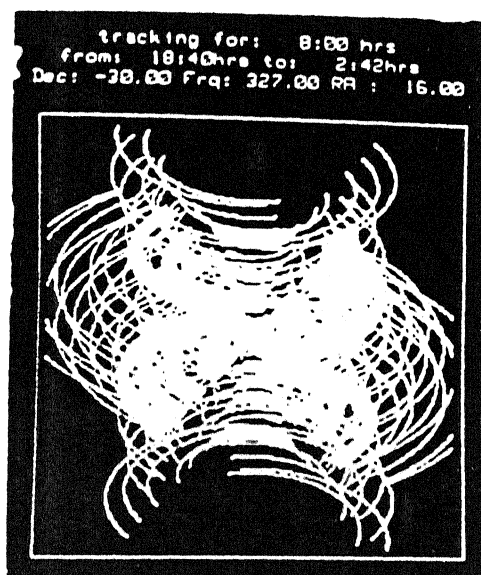


Fig. 4.1(a)

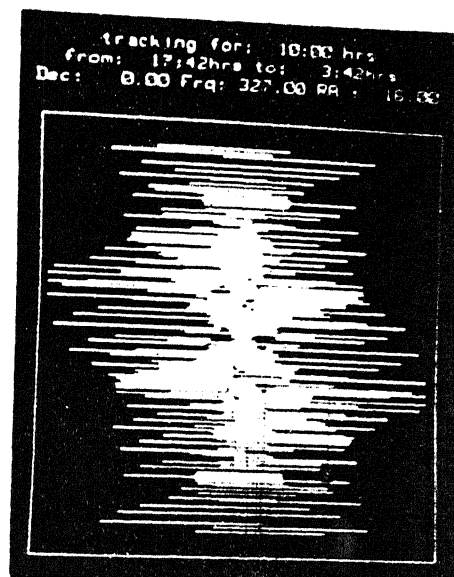


Fig. 4.1(b)

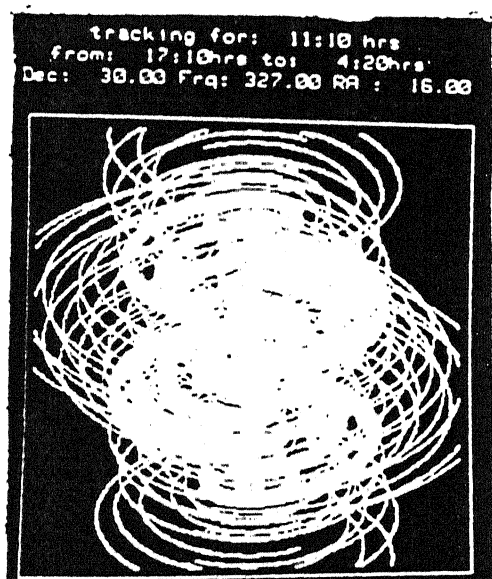


Fig. 4.1(c)

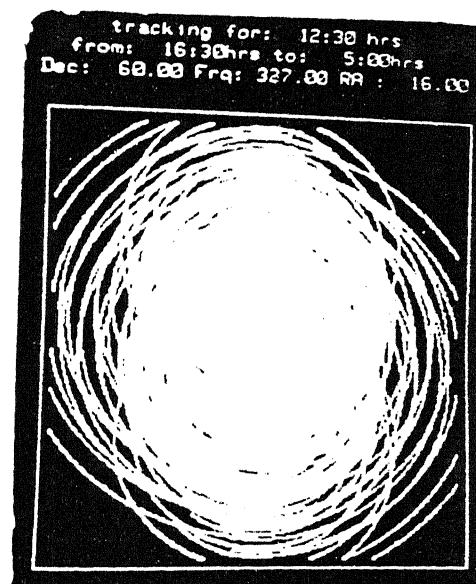


Fig. 4.1(d)

Fig. 4.1(a) :  $U(u,v)$  function for 327 MHz at  $\delta = -30^\circ$   
 (b) :  $U(u,v)$  function for 327 MHz at  $\delta = 0^\circ$   
 (c) :  $U(u,v)$  function for 327 MHz at  $\delta = 30^\circ$   
 (d) :  $U(u,v)$  function for 327 MHz at  $\delta = 60^\circ$

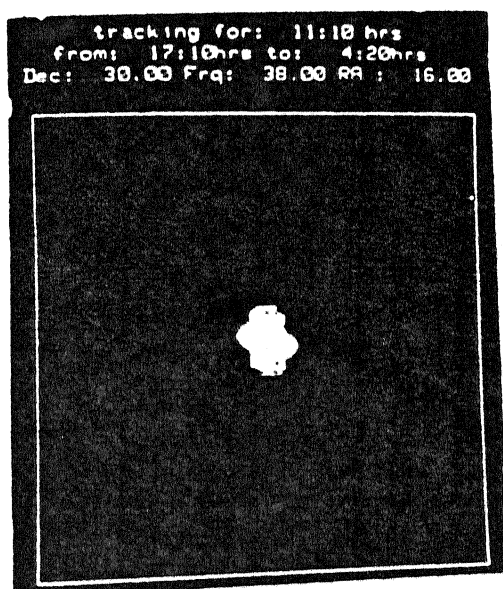


Fig. 4.1(e)

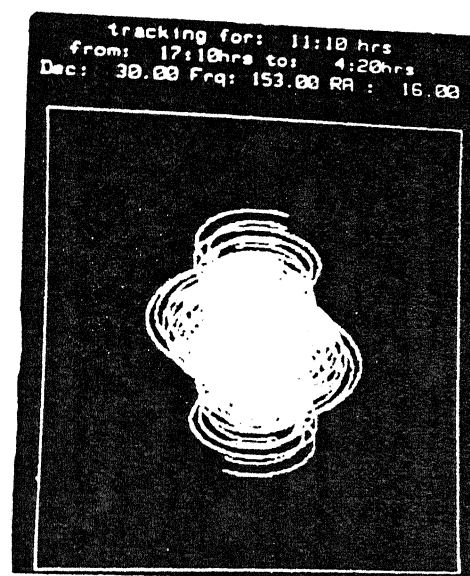


Fig. 4.1(f)

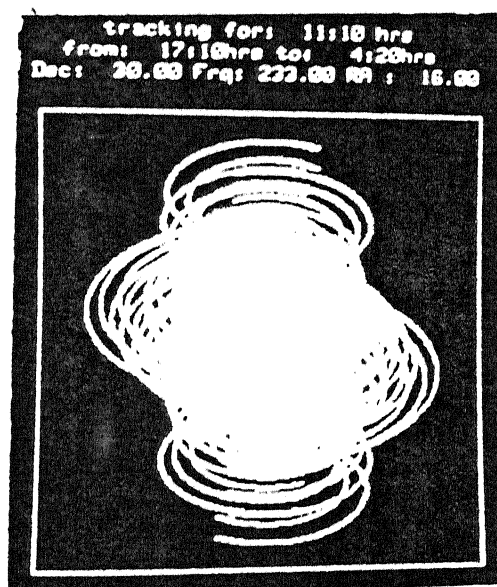


Fig. 4.1(g)



Fig. 4.1(h)

Fig. 4.1(e) :  $U(u,v)$  function for 38 MHz at  $\delta = 30^\circ$   
 (f) :  $U(u,v)$  function for 153 MHz at  $\delta = 30^\circ$   
 (g) :  $U(u,v)$  function for 233 MHz at  $\delta = 30^\circ$   
 (h) :  $U(u,v)$  function for 611 MHz at  $\delta = 30^\circ$



unsampled point are a major source of distortion introduced in the reconstructed image.

We have taken the model images to consist of 256 x 256 grid points which together constitute a 20' x 20' image.

The following formulae are used for calculation of  $u$  and  $v$  (Mathur, 1969).

$$b_1 = (D/\lambda) \cdot (y_1 - y_2) \cdot \cos \phi \quad (4.1)$$

$$b_2 = (D/\lambda) \cdot (y_1 - y_2) \cdot \sin \phi \quad (4.2)$$

$$u = b_2 \sin H \quad (4.3)$$

$$v = b_1 \cos \delta - b_2 \sin \delta \cos H \quad (4.4)$$

where  $\delta$  = declination of the source,

$H$  = hour angle of the source,

$\phi$  = latitude of the telescopic site

$D$  = baseline length

$$= \sqrt{(x_1 - x_2)^2 + (y_1 - y_2)^2 + (z_1 - z_2)^2}$$

$(x, y, z)$  define the coordinates of antennas forming the interferometer, with  $(x, y)$  being measured in a plane parallel to the earth's equator,  $x$  in the meridian plane,  $y$  towards the east and  $z$  is measured towards the celestial north pole (Fig. 2.6). The tracking of source is done for all the time the source has an elevation angle greater than fifteen degrees. The calculations for  $u$  and  $v$  are done after intervals of 1 min. This interval has been fixed by taking into account the speed of coverage of the

u-v plane by the u-v ellipses. A compromise has to be worked between the facts that more frequent samples may result in the points lying in the same grid whereas less frequent calculation may end up missing some intermediate grid points through which the ellipse passes. A 128 x 256 array is used to store the number of times each (u,v) cell is sampled. The cells which are not sampled are assigned a value of zero. Use is made of the fact that,

$$V(u,v) = V^*(-u, -v)$$

So whenever a point (u,v) is sampled, the corresponding point (-u, -v) is also sampled.

The major source of distortion in reconstructed images is the existence of unsampled cells in the u-v plane. The  $W(u,v)$  function tells us the extent of u-v plane coverage. Fig. 4.1 gives us an idea of the  $W(u,v)$  function for different declinations and frequencies for the GMRT 30 element array. The configuration of the GMRT array is given in Fig. 4.2 (Swarup, 1990) and the co-ordinates of the various antennas are given in Table 4.1.

The second part is a routine for the calculation of the structure function which is used for calculation of the ionospheric effect  $I(u,v)$  as explained earlier.

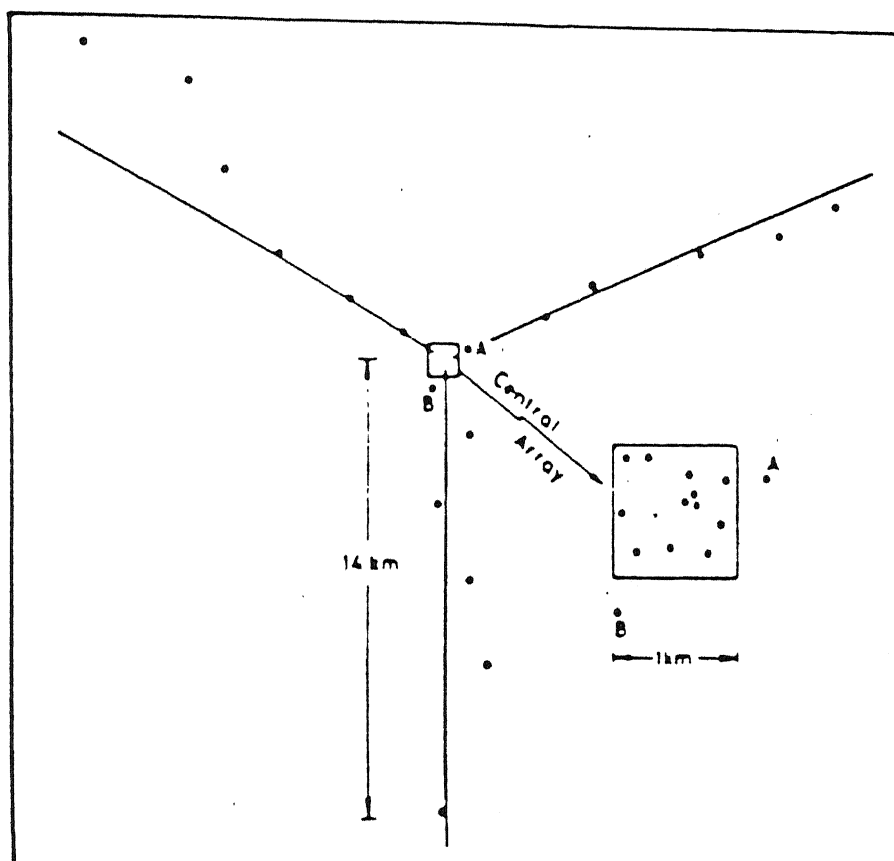


Fig. 4.2 : Array configuration of giant metrewave radio telescope (GMRT), consisting of 30 nos. of 45-m diameter steerable dishes.

TABLE 4.1 : The GMRT antenna array co-ordinates in metres

Antenna	X	Y	Z
1.	-258.0	259.0	33.0
2.	802.0	94.0	39.0
3.	103.0	237.0	35.0
4.	237.0	259.0	37.0
5.	998.0	104.0	40.0
6.	360.0	497.0	42.0
7.	461.0	469.0	43.0
8.	149.0	659.0	49.0
9.	386.0	396.0	44.0
10.	600.0	850.0	45.0
11.	1034.0	575.0	47.0
12.	266.0	907.0	15.0
13.	847.0	1380.0	17.0
14.	903.0	899.0	19.0
15.	-2690.0	-800.0	53.0
16.	11610.0	-9250.0	01.0
17.	-4190.0	-1750.0	55.0
18.	-7590.0	-2750.0	58.0
19.	-10090.0	-3350.0	61.0
20.	-11890.0	-4300.0	63.0
21.	-290.0	2750.0	31.0
22.	760.0	4950.0	21.0
23.	-240.0	7150.0	29.0
24.	-790.0	9750.0	23.0
25.	660.0	14400.0	25.0
26.	1810.0	-300.0	13.0
27.	3510.0	-1300.0	11.0
28.	5710.0	-2600.0	09.0
29.	7310.0	-5200.0	07.0
30.	8410.0	-8000.0	05.0

The subroutine ION calculates the factor

$$I(u,v) = \exp(-D\phi/2)$$

This subroutine makes use of the anisotropic ionospheric irregularity model developed by Fremouw and Secan (1984) for their WBMOD program for calculation of ionospheric scintillation indices. The inputs to the program required are :

- i) Time of the day (Diurnal effect)
- ii) Elevation angle
- iii) Azimuth angle
- iv) Sun spot number
- v) The planetary magnetic index  $K_p$ .

For relating the time of the day to the hour angle of the source we have made use of the relations

$$\text{Local civil time (LCT)} = \text{Local sidereal time (LST)} - \frac{69}{70} \times 4^m \times D \quad (4.5)$$

$$\text{LST} = \text{R.A. of source } (\alpha) + \text{Local hour angle (LHA)} \quad (4.6)$$

so that

$$\text{LCT} = \alpha + \text{LHA} - \frac{4}{60} \times \frac{69}{70} D \text{ (hrs.)} \quad (4.7)$$

where  $D$  = Day of the year reckoned from the 264.7<sup>th</sup> day of the year (September 21<sup>st</sup>) which is the autumnal equinox.

Using the standard relations for relating the azimuth angle and the elevation angle to the hour angle, we can for each sample calculate the value of  $I(u,v)$ . A  $256 \times 256$  array (KDATA) stores the value of  $I(u,v)$  in the proper grid position. For each new sample corresponding to the  $(u_1, v_1)$  point, the value in that KDATA cell is incremented by  $I(u_1, v_1)$ . After the completion of the tracking, the average value of the measured visibility function is calculated by dividing the values of KDATA array by the corresponding total number of samples. The unsampled points are assigned a value of zero.

When there is no ionospheric effect, we have a  $256 \times 256$  array filled with 1's and 0's corresponding to the sampled and unsampled points. Now a uniform gaussian taper of 15 dB at the edges is applied and the inverse FFT is calculated to get the reconstructed image from the Fourier transform of the original assumed source distribution.

For the KDATA array, the same procedure leaves us with an array filled with zeroes corresponding to unsampled points and values different from zero for the sampled points. After applying the gaussian taper and performing the inverse FFT we get the reconstructed image with the effect of the ionosphere.

The dB errors - maximum and r.m.s. for images A, B and C are calculated for different regions surrounding the source. For the purpose of calculations a point source and an extended source have been considered.

## CHAPTER 5

### RESULTS AND CONCLUSION

The effect of following parameters on the reconstructed image were studied

- a) The size of the assumed source brightness distribution
- b) Declination of the source
- c) Frequency of observation
- d) Right ascension of source
- e) Solar activity in terms of sun spot number
- f) The season of the year.

Table 0 lists the figure and quantitative data table numbers for the different parameters for which study has been conducted. Note that Plot-A corresponds to the assumed source distribution, B to the reconstructed source distribution without the effect of ionosphere and C to the reconstructed source distribution with the effect of ionosphere. The Fig. 5.1 gives the Plot-A for the point source and Fig. 5.2 for an extended gaussian source with the 3 dB half width of 60 arc-seconds. The planetary magnetic index has been kept at a typical value of 4.0 since dependence on this parameter is very weak.

#### 5.1 EFFECT OF SIZE OF SOURCE

Two types of source distributions were studied

- a) Point source brightness distribution
- b) Extended gaussian source brightness distribution.

Table 0 : List of various figures and tables for different parameters

Fig.	Table	Source	SSN	K <sub>p</sub>	Day	$\delta$ (degrees)	Freq. (MHz)	RA (hours)
1	-	Point						
2	-	Extended						
3	1	Point	50	4	170	-30	38	1600
4	2	Point	50	4	170	0	38	1600
5	3	Point	50	4	170	30	38	1600
6	4	Point	50	4	170	60	38	1600
7	5	Point	50	4	170	0	153	1600
8	6	Point	50	4	170	30	153	1600
9	7	Point	50	4	170	30	38	0800
10	8	Point	200	4	170	30	38	1600
11	9	Extended	50	4	170	30	38	1600
12	10	Extended	50	4	170	0	153	1600
13	11	Extended	200	4	170	30	38	1600
14	12	Point	50	4	170	30	232	1600
15	13	Point	50	4	170	30	327	1600
16	14	Extended	50	4	170	30	327	1600
17	15	Extended	50	4	70	30	38	1600
18	16	Extended	50	4	70	30	38	0800

SSN = Sun Spot Number

K<sub>p</sub> = Planetary Magnetic Index

Day = 70 (March)  
= 170 (June)

RA = Right Ascension

$\delta$  = Declination



In general, spurious structure are introduced into the reconstructed images even without the effect of the ionosphere being considered. This spurious structure is introduced due to the truncation of the sample space based on maximum baseline available, measurement at discrete intervals and existence of unsampled points in the  $u$ - $v$  plane.

There is stretching of the reconstructed source image, roughly along constant right ascension axes. The reconstructed image which includes the effect of the ionosphere is broadened in a direction perpendicular to the direction of stretching of the reconstructed image without the effect of the ionosphere. This is borne out quite clearly in the Figs. 5.4 and 5.6.

The rms distortion in an area of radius 30 arc seconds is less than 3 dBs for the point source and is less than 2 dB for the extended source even within an area of 60 arc-seconds. For an extended source, the distortion levels are very small. The distortion level  $\simeq 0$  dBs upto a radius of  $\simeq 60$  arc-seconds which is to be expected for a source with a 3 dB half width of  $\simeq 60$  arc-seconds. For very severe cases of distortion one cannot even distinguish between a point source and extended source as is seen from Figs. 5.5 and 5.11 and Figs. 5.7 and 5.12.

## 5.2 EFFECT OF DECLINATION OF SOURCE

Two effects are observed.

- i) The increased tracking time for higher declinations leads to greater fidelity reconstructed images
- ii) Tracking at large zenith angles for larger portion of time leads to greater distortion.

These two effects are opposing in nature and are seen clearly from plots in Figs. 5.3, 5.4, 5.5 and 5.6, which correspond to declinations of  $-30$ ,  $0$ ,  $30$  and  $60$ , respectively.

The better fidelity can be seen from smaller r.m.s. error between plots (A-B) for increasing declination and the greater distortion can be seen from the increasing r.m.s. error between plots (B-C) and (A-C) as seen from Tables 1, 2, 3 and 4.

## 5.3 EFFECT OF FREQUENCY

As is to be expected, there is increasing distortion with decreasing frequency. The effect of ionosphere at a declination of  $30^\circ$  can be clearly seen in Figs. 5.5, 5.8, 5.14, 5.15 (corresponding to frequencies of 38, 153, 232 and 327 MHz respectively) with Figs. 5.15 and 5.16 showing the comparative effects on point and extended source, respectively at 327 MHz.

#### 5.4 EFFECT OF RIGHT ASCENSION

The RA determines the time of the day, during which the source is being tracked. Since the maximum scintillation occurs around 22:30 hours local time, we expect maximum distortion to take place for images which are produced by tracking around this time. This is infact true as is borne out by Figs. 5.5 and 5.9 for a point source. Tables 3 and 7 also bring out these factors quantitatively.

#### 5.5 EFFECT OF SEASON

The seasonal scintillation maxima occur during March and October and minima around December and June. Hence, we expect the results to change accordingly. Figs. 5.11, 5.17 and 5.18 show the effect of the effect of season on an extended source at 38 MHz. Figure 5.18 shows the effect of the season for the same parameters except inclusion of the night time maxima. There is greater stretching of 6 dB lobes along the constant RA axes. This implies greater distortion of the image, even though this may not be reflected in the corresponding quantitative figures.

#### 5.6 EFFECT OF SUN SPOT NUMBER (SSN)

The magnetic activity is parameterised in terms of the sun spot number. There is no appreciable difference as is shown in Figs. 5.5 & 5.10 (for SSN = 50 and 200 at 153 MHz) and Figs. 5.11 & 5.13 (for SSN = 50 and 200 at 38 MHz) together with the

CENTRAL LIBRARY  
I. I. T. KANPUR  
113546

corresponding quantitative errors in Tables 3, 8, 9 and 11. This is to be expected as there is very weak relationship between scintillation strength and magnetic activity.

## 5.7 CONCLUSION

There would be large distortion for 38 MHz and 153 MHz reconstructed images. The images of sources, both point and extended will be extended, more or less in a direction parallel to axes of constant right ascension. For month of March and October, it will be very difficult to distinguish between point and extended source and we might as well discard data for higher declinations for these months. This is true even for data which may not include the night-time scintillation maxima.

There is only a small effect of scintillation on the 233 MHz and other higher frequency observations and we can safely neglect these effects.

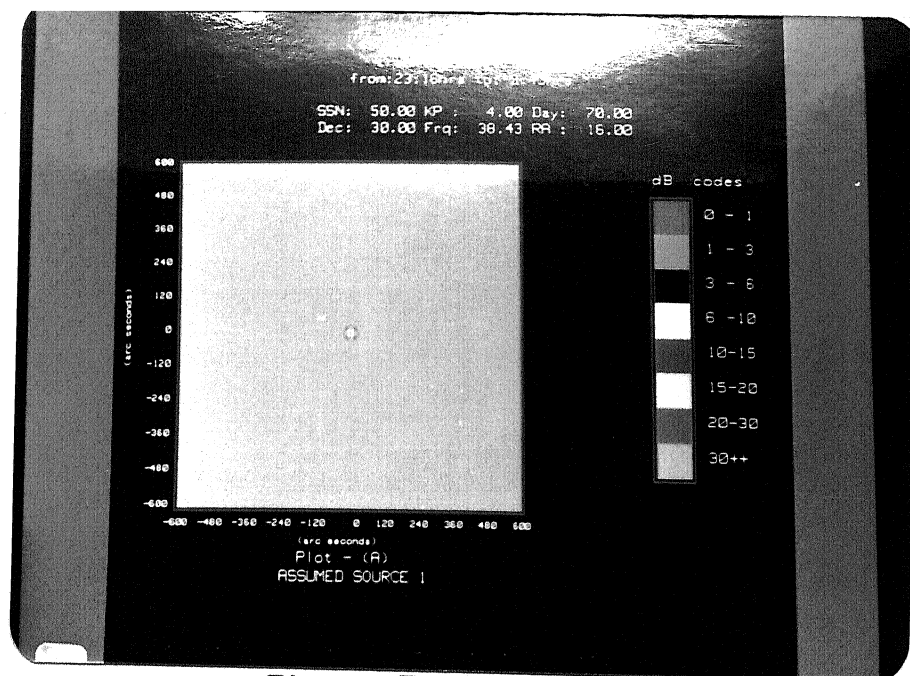


Figure 5.1(a)

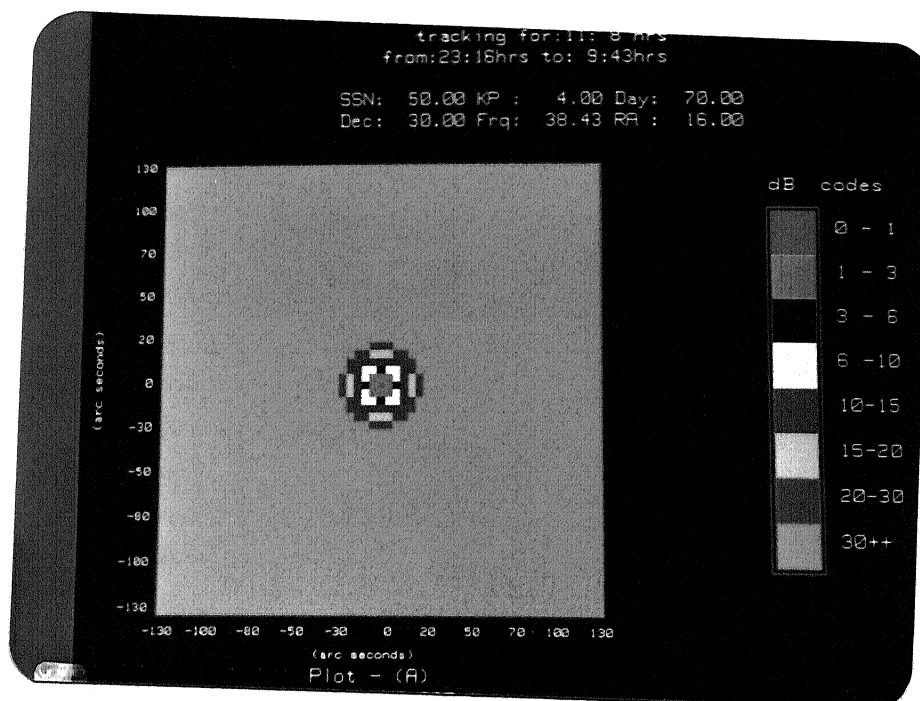


Figure 5.1(b)

Fig. 5.1 : (a) Assumed point source distribution  
(b) A blown out view of source in (a)

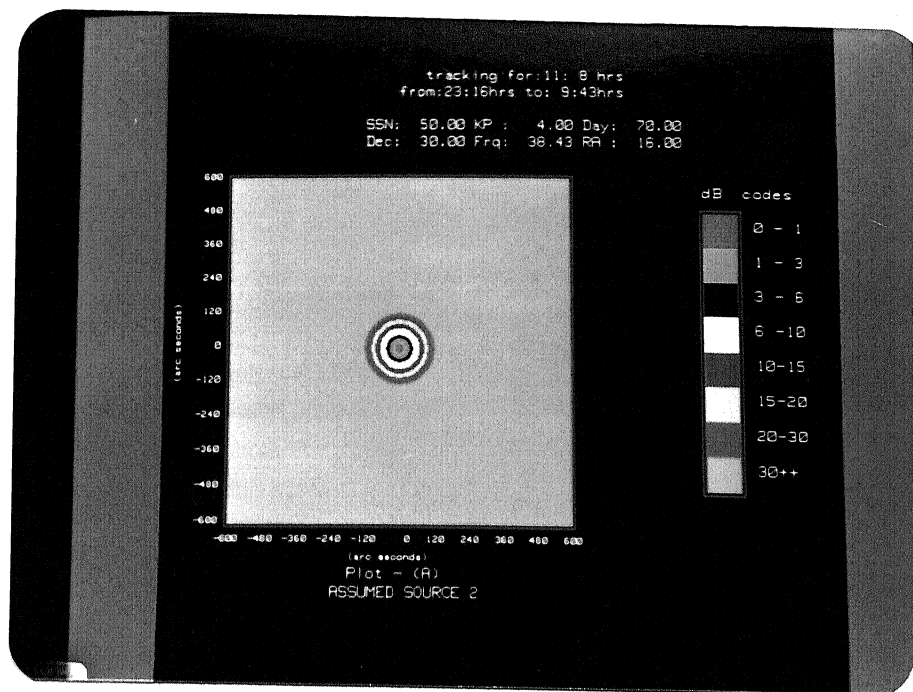


Figure 5.2(a)

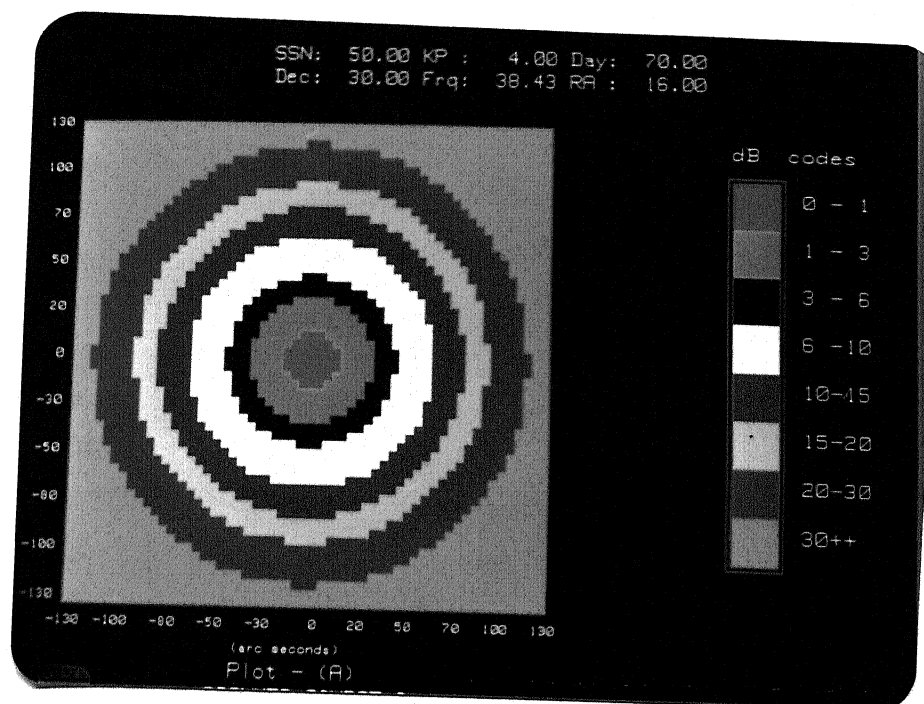


Figure 5.2(b)

Fig. 5.2 : (a) Assumed extended gaussian source distribution  
(b) A blown out view of source in (a)

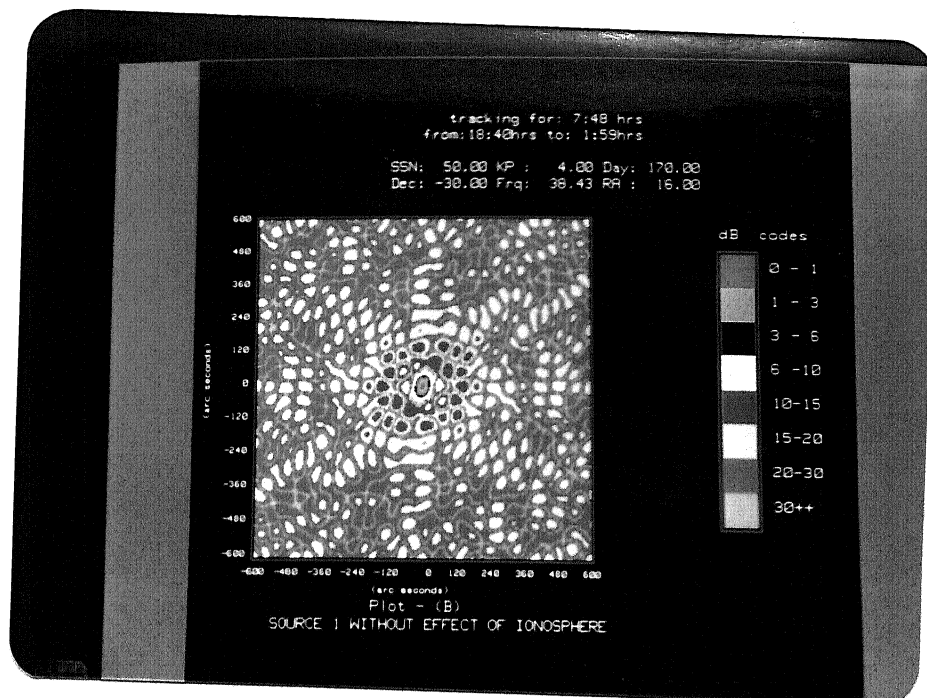


Fig. 5.3(a) : Plot-B corresponding to Plot-A of Fig. 5.1.

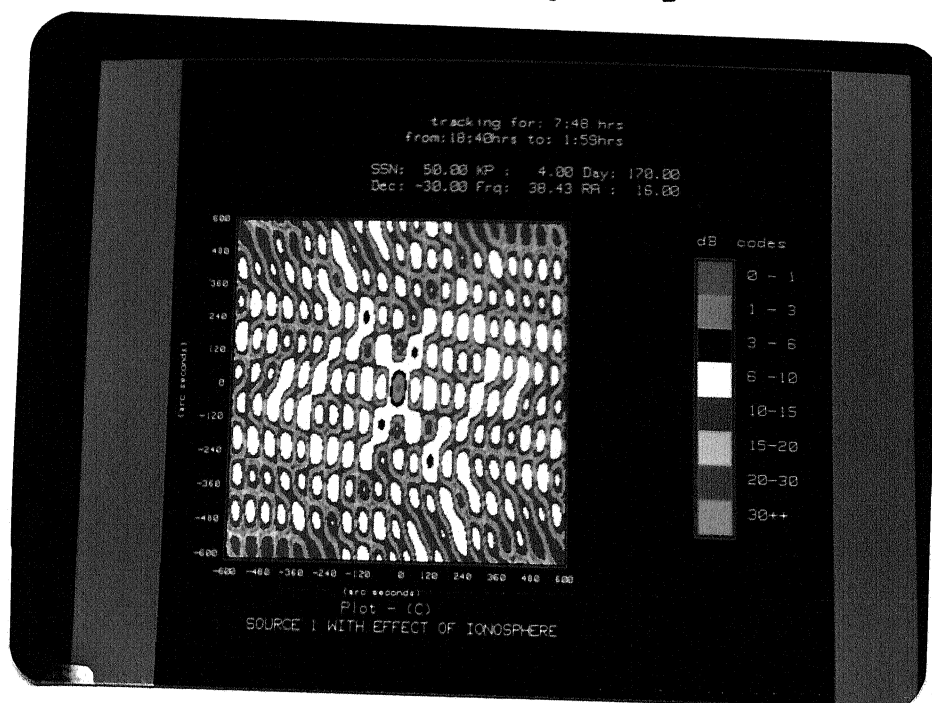


Fig. 5.3(b) : Plot-C corresponding to Plot-A of Fig. 5.1.

Region	A-B		A-C		B-C	
	max	rms	max	rms	max	rms
0-30"	9.0	3.7	9.0	3.8	1.0	0.3
0-60"	19.0	10.9	19.0	11.2	1.0	0.5
0-120"	33.0	20.9	33.0	21.1	1.0	0.6
0-300"	75.0	47.7	77.0	48.6	4.0	1.5
0-600"	87.0	50.4	90.0	53.7	23.0	5.8

Table 1 : dB Errors for Plots of Fig. 5.3

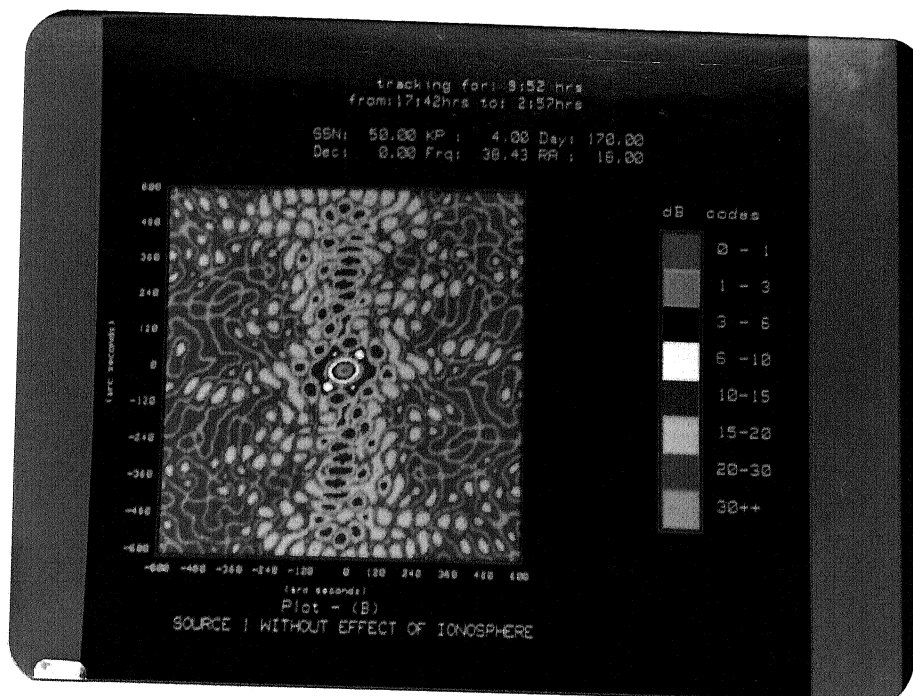


Fig. 5.4(a) : Plot-B corresponding to Plot-A of Fig. 5.1.

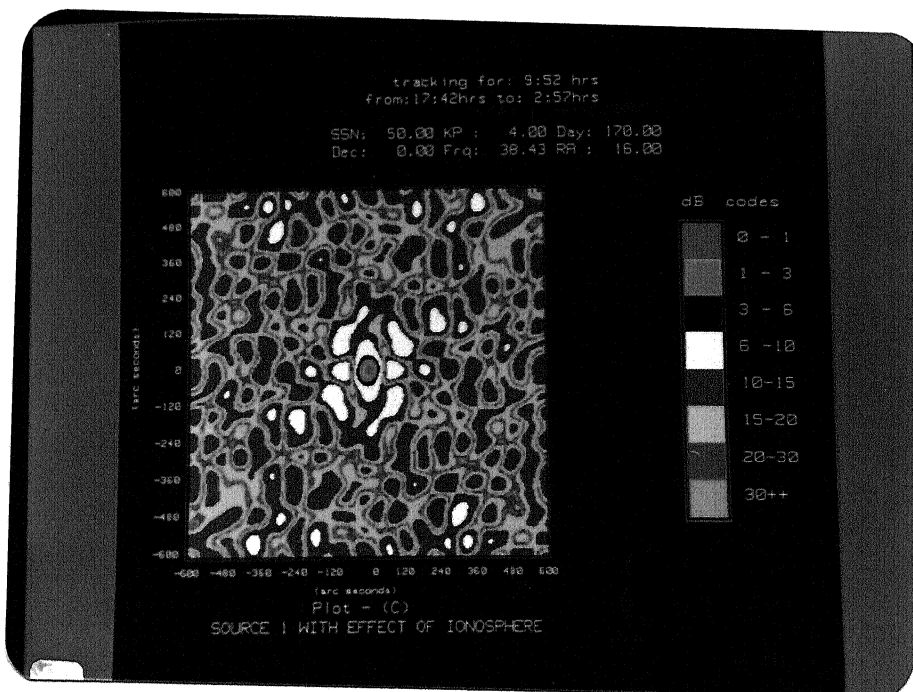


Fig. 5.4(b) : Plot-C corresponding to Plot-A of Fig. 5.1.

Region	A-B		A-C		B-C	
	max	rms	max	rms	max	rms
0-30"	8.0	3.7	9.0	3.8	1.0	0.3
0-60"	19.0	10.9	19.0	11.3	1.0	0.7
0-120"	33.0	20.9	34.0	21.5	2.0	0.9
0-300"	75.0	48.0	77.0	49.8	6.0	2.3
0-600"	87.0	50.7	89.0	55.0	20.0	7.9

Table 2 : dB Errors for Plots of Fig. 5.4



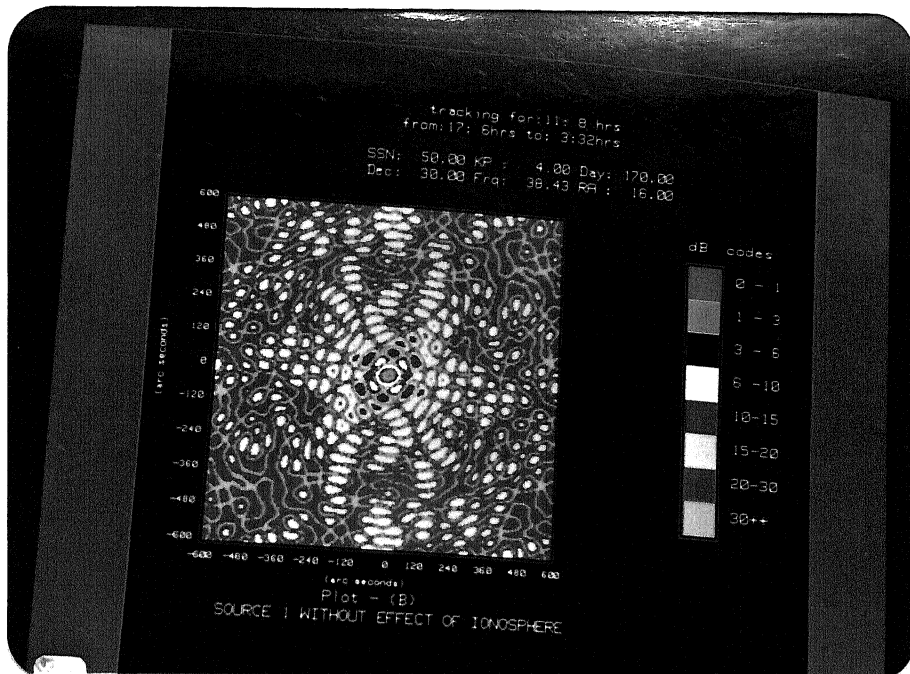


Fig. 5.5(a) : Plot-B corresponding to Plot-A of Fig. 5.1.

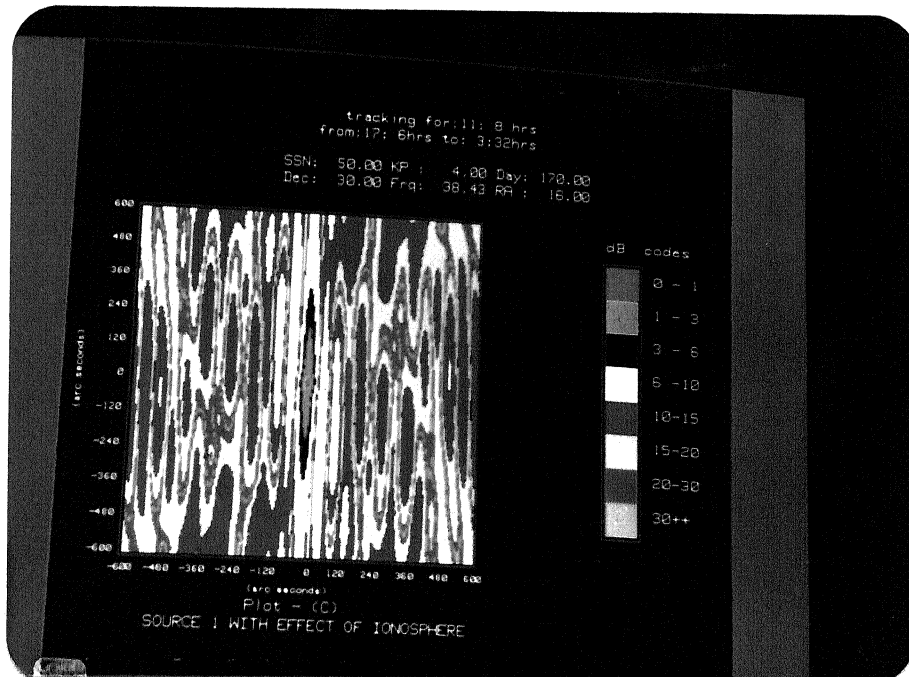


Fig. 5.5(b) : Plot-C corresponding to Plot-A of Fig. 5.1.

Region	A-B		A-C		B-C	
	max	rms	max	rms	max	rms
0-30"	8.0	3.6	9.0	3.8	1.0	0.4
0-60"	18.0	10.8	19.0	11.2	2.0	0.8
0-120"	32.0	20.4	33.0	21.1	2.0	1.2
0-300"	72.0	46.0	77.0	48.6	16.0	4.5
0-600"	83.0	48.3	90.0	53.3	22.0	9.3

Table 3 : dB Errors for Plots of Fig. 5.5

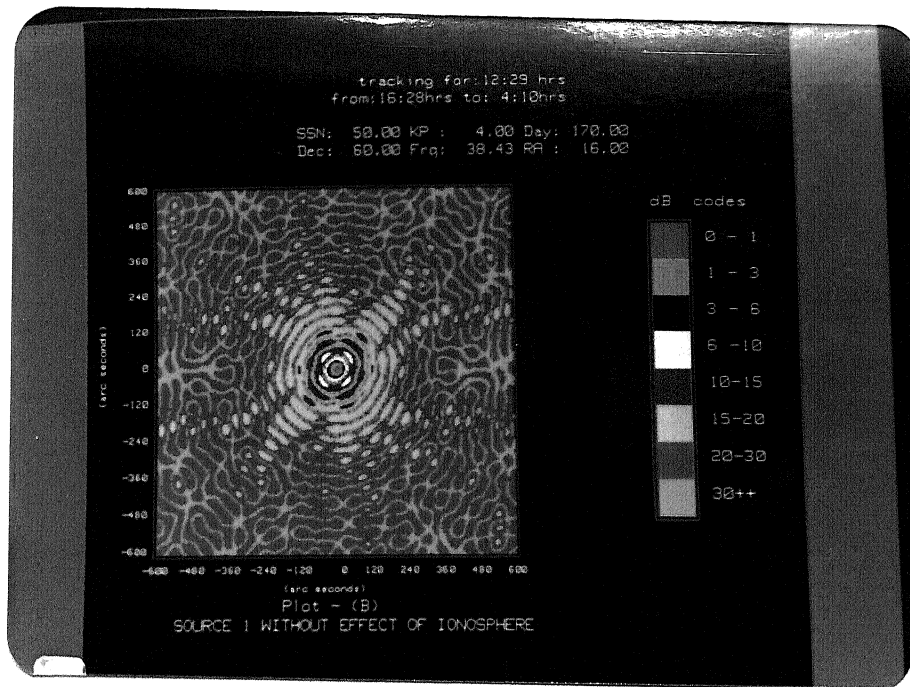


Fig. 5.6(a) : Plot-B corresponding to Plot-A of Fig. 5.1.

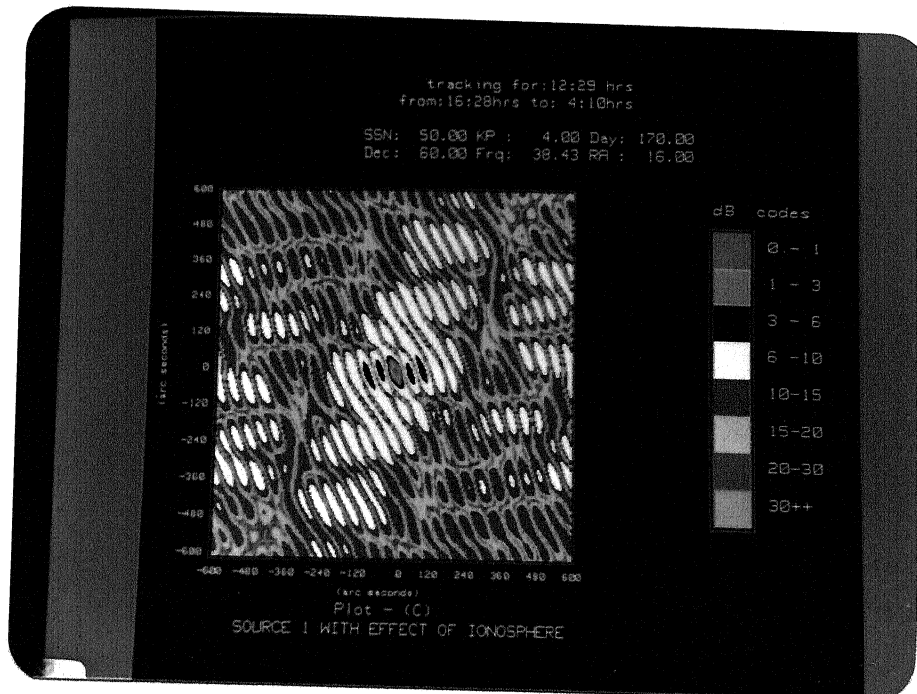


Fig. 5.6(b) : Plot-C corresponding to Plot-A of Fig. 5.1.

Region	A-B		A-C		B-C	
	max	rms	max	rms	max	rms
0-30"	8.0	3.5	8.0	3.5	1.0	0.6
0-60"	18.0	10.7	17.0	10.7	1.0	0.8
0-120"	32.0	20.3	28.0	19.9	5.0	1.7
0-300"	71.0	46.1	75.0	46.3	16.0	5.1
0-600"	79.0	47.4	89.0	54.5	25.0	9.2

Table 4 : dB Errors for Plots of Fig. 5.6

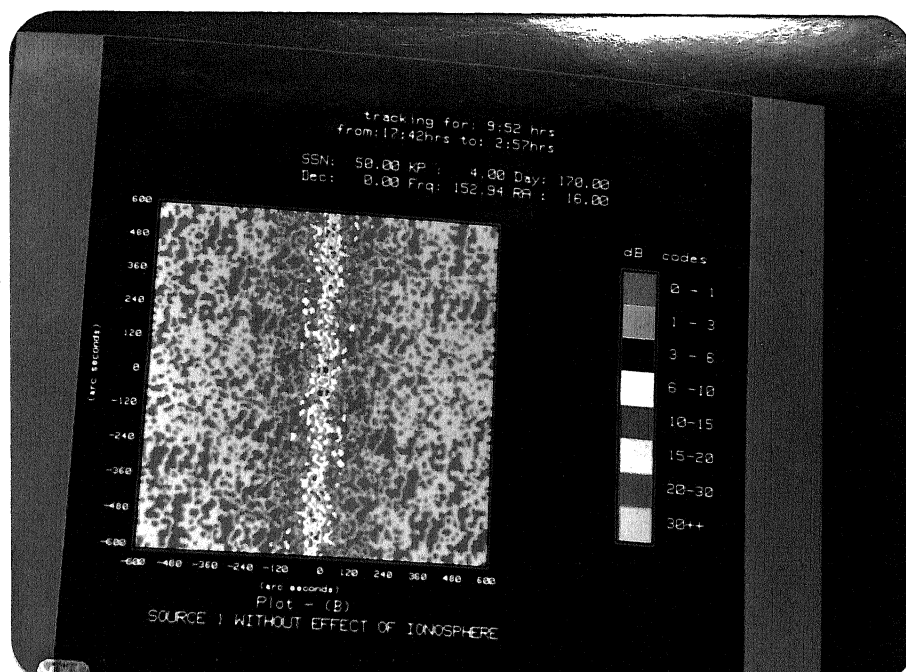


Fig. 5.7(a) : Plot-B corresponding to Plot-A of Fig. 5.1.

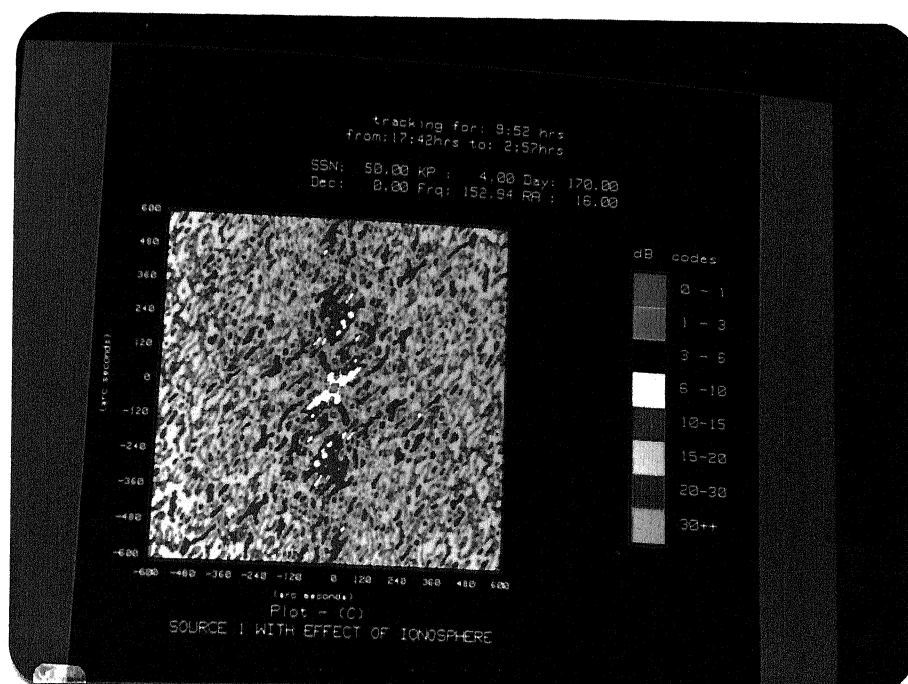


Fig. 5.7(b) : Plot-C corresponding to Plot-A of Fig. 5.1.

Region	A-B		A-C		B-C	
	max	rms	max	rms	max	rms
0-30"	5.0	2.0	7.0	2.6	2.0	0.9
0-60"	11.0	6.1	16.0	7.6	6.0	2.4
0-120"	18.0	10.0	30.0	15.0	18.0	8.0
0-300"	66.0	36.1	75.0	42.8	27.0	10.1
0-600"	81.0	44.0	87.0	49.4	35.0	9.5

Table 5 : dB Errors for Plots of Fig. 5.7

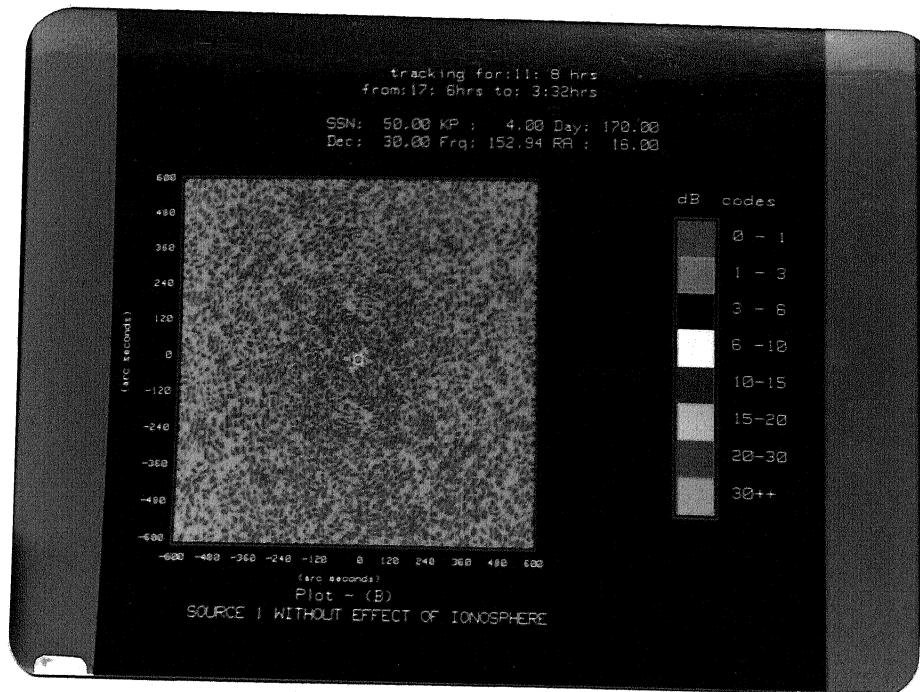


Fig. 5.8(a) : Plot-B corresponding to Plot-A of Fig. 5.1.

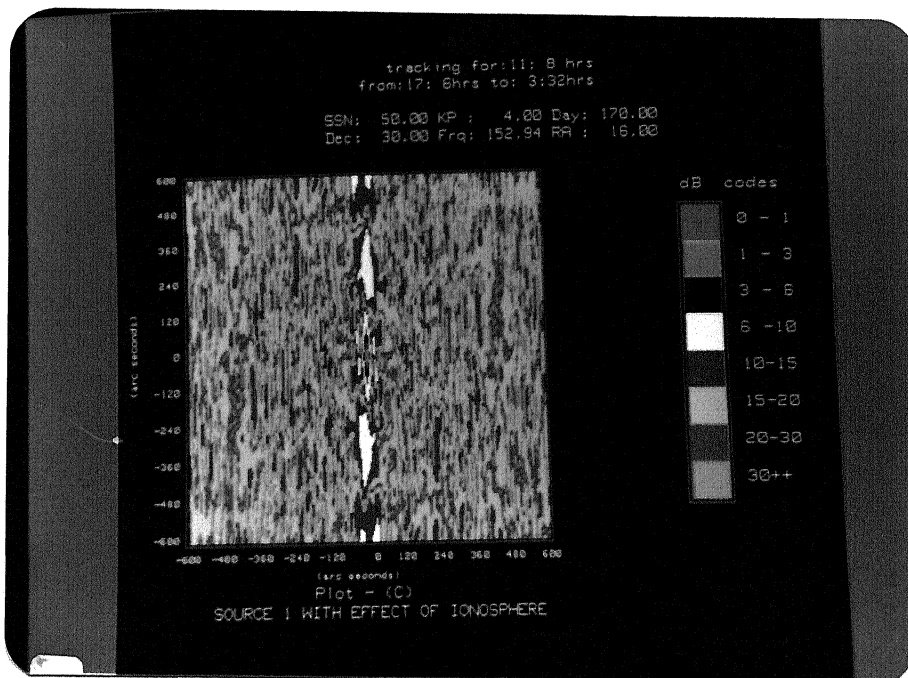


Fig. 5.8(b) : Plot-C corresponding to Plot-A of Fig. 5.1.

Region	A-B		A-C		B-C	
	max	rms	max	rms	max	rms
0-30"	4.0	1.6	5.0	2.2	2.0	1.0
0-60"	6.0	4.3	16.0	7.2	11.0	4.0
0-120"	15.0	7.0	26.0	14.9	28.0	9.7
0-300"	63.0	31.2	72.0	42.3	28.0	13.6
0-600"	72.0	38.4	86.0	48.0	31.0	13.6

Table 6 : dB Errors for Plots of Fig. 5.8

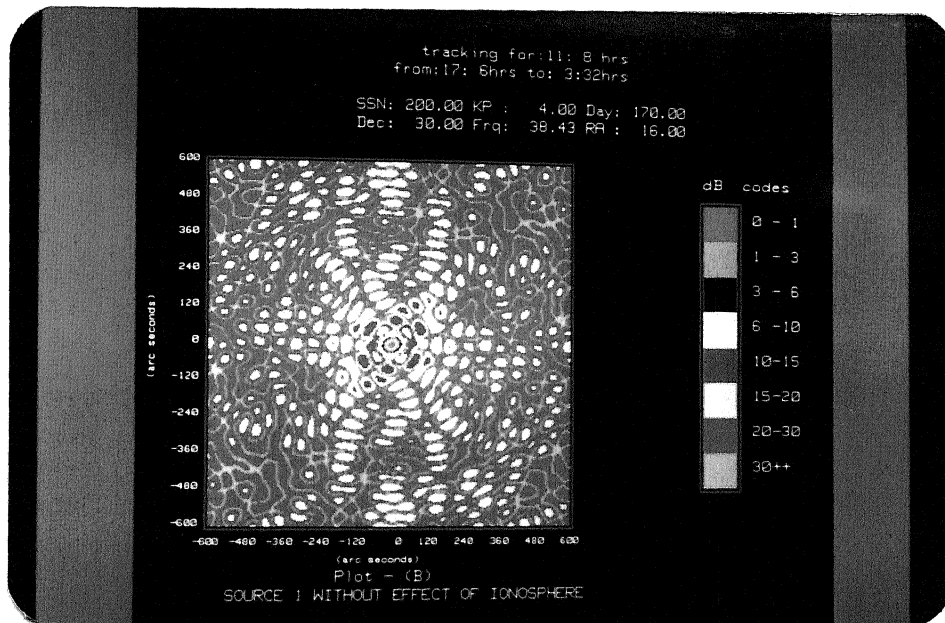


Fig. 5.10(a) : Plot-B corresponding to Plot-A of Fig. 5.1.

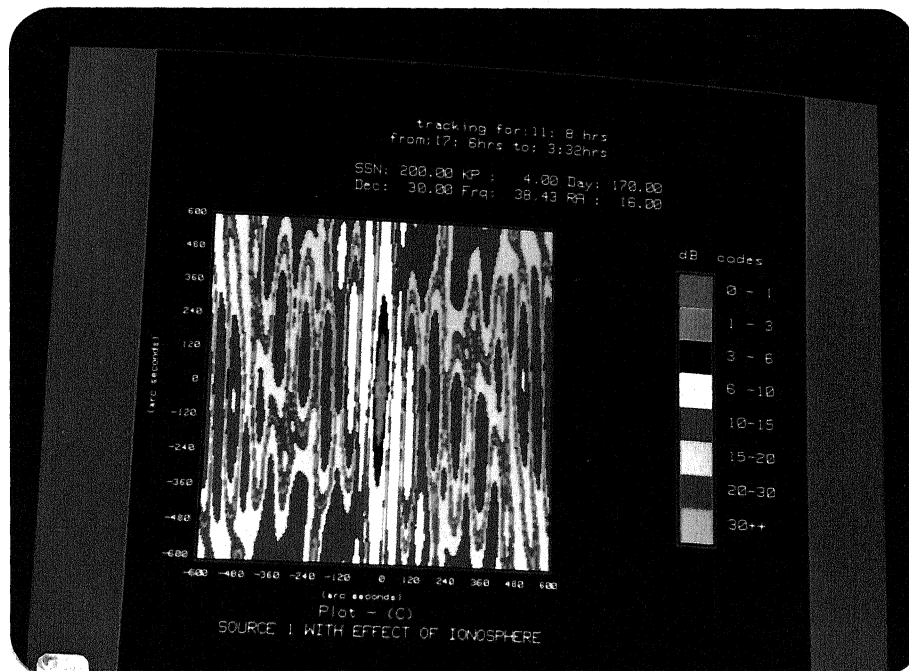


Fig. 5.10(b) : Plot-C corresponding to Plot-A of Fig. 5.1.

Region	A-B		A-C		B-C	
	max	rms	max	rms	max	rms
0-30"	8.0	3.6	9.0	3.8	1.0	0.4
0-60"	18.0	10.8	19.0	11.2	2.0	0.8
0-120"	32.0	20.4	33.0	21.1	2.0	0.2
0-300"	72.0	46.3	77.0	48.6	16.0	4.4
0-600"	83.0	48.3	90.0	53.3	22.0	9.3

Table 8 : dB Errors for Plots of Fig. 5.10

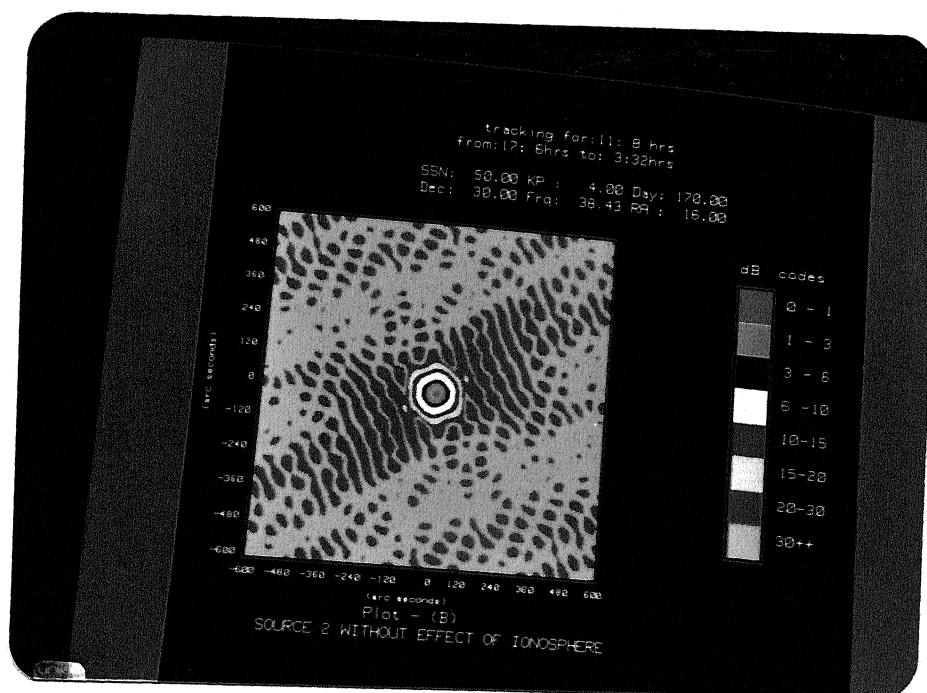


Fig. 5.11(a) : Plot-B corresponding to Plot-A of Fig. 5.2.

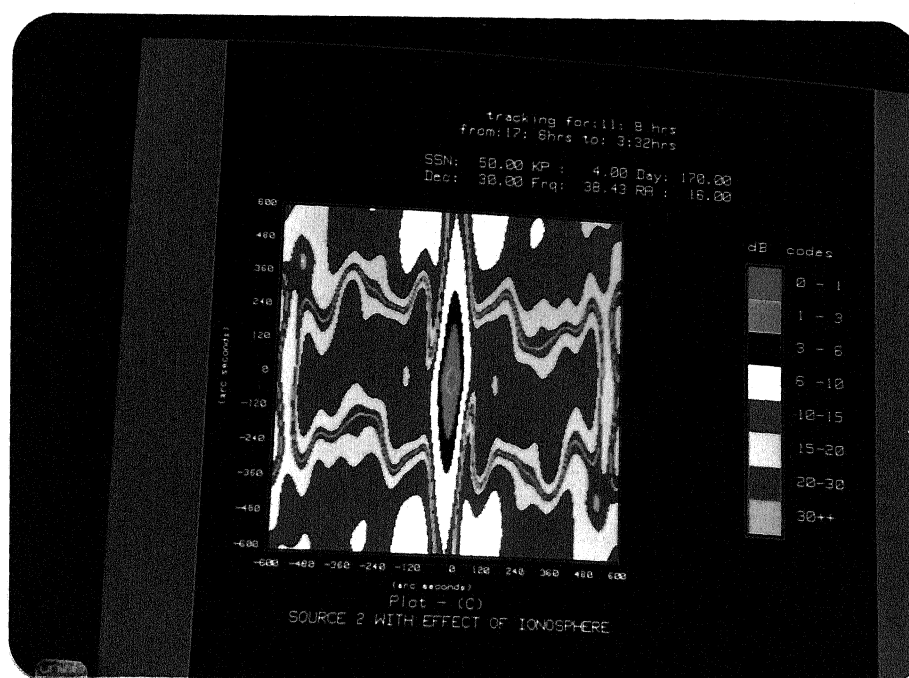


Fig. 5.11(b): Plot-C corresponding to Plot-A of Fig. 5.2.

Region	A-B		A-C		B-C	
	max	rms	max	rms	max	rms
0-30"	0.0	0.0	0.0	0.0	0.0	0.0
0-60"	1.0	0.2	1.0	0.5	1.0	0.5
0-120"	1.0	0.2	1.0	0.7	1.0	0.7
0-300"	1.0	0.4	3.0	1.2	3.0	1.1
0-600"	1.0	0.5	5.0	2.2	5.0	2.1

Table 9 : dB Errors for Plots of Fig. 5.11



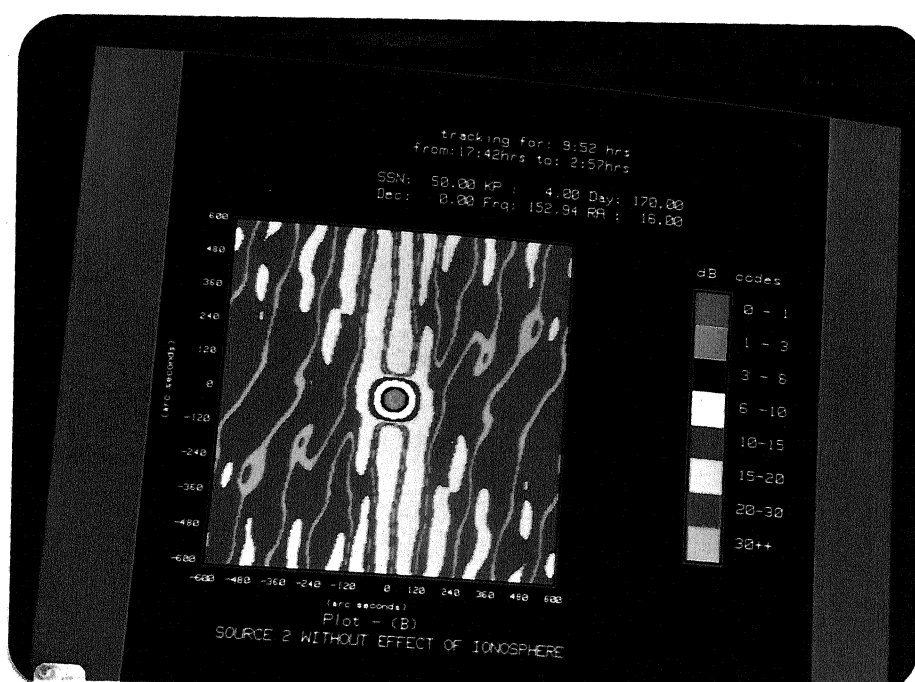


Fig. 5.12(a) : Plot-B corresponding to Plot-A of Fig. 5.2.

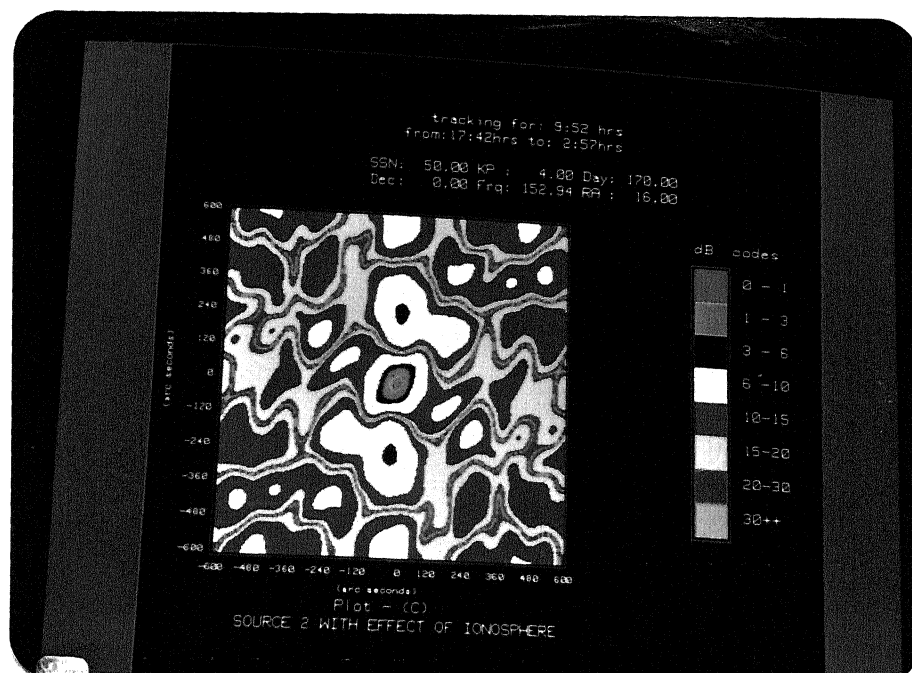


Fig. 5.12(b) : Plot-C corresponding to Plot-A of Fig. 5.2.

Region	A-B		A-C		B-C	
	max	rms	max	rms	max	rms
0-30"	0.0	0.0	0.0	0.0	0.0	0.0
0-60"	0.0	0.0	1.0	0.6	1.0	0.6
0-120"	0.0	0.0	1.0	0.6	1.0	0.6
0-300"	1.0	0.3	2.0	1.2	2.0	1.0
0-600"	1.0	0.5	4.0	2.1	4.0	2.0

Table 10 : dB Errors for Plots of Fig. 5.12

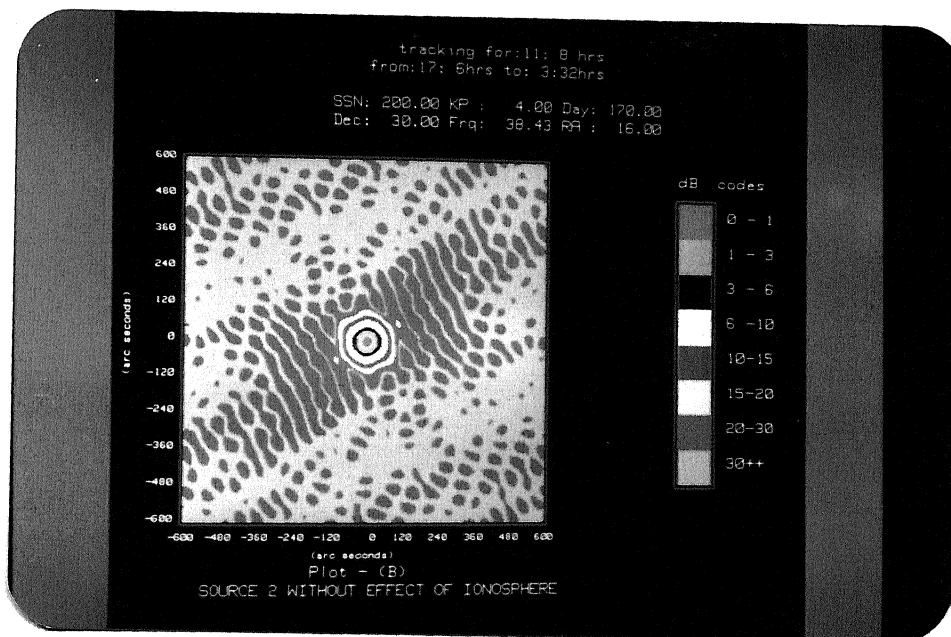


Fig. 5.13(a) : Plot-B corresponding to Plot-A of Fig. 5.2.

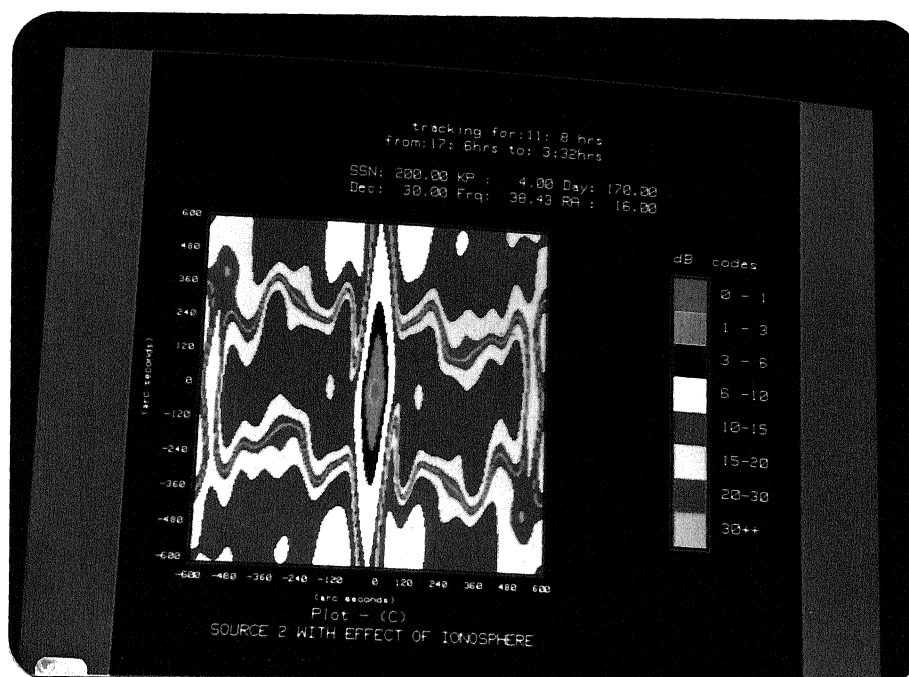


Fig. 5.13(b): Plot-C corresponding to Plot-A of Fig. 5.2.

Region	A-B		A-C		B-C	
	max	rms	max	rms	max	rms
0-30"	0.0	0.0	0.0	0.0	0.0	0.0
0-60"	1.0	0.2	1.0	0.5	1.0	0.5
0-120"	1.0	0.2	1.0	0.7	1.0	0.7
0-300"	1.0	0.4	3.0	1.2	3.0	1.1
0-600"	1.0	0.5	5.0	2.3	5.0	2.1

Table 11 : dB Errors for Plots of Fig. 5.13



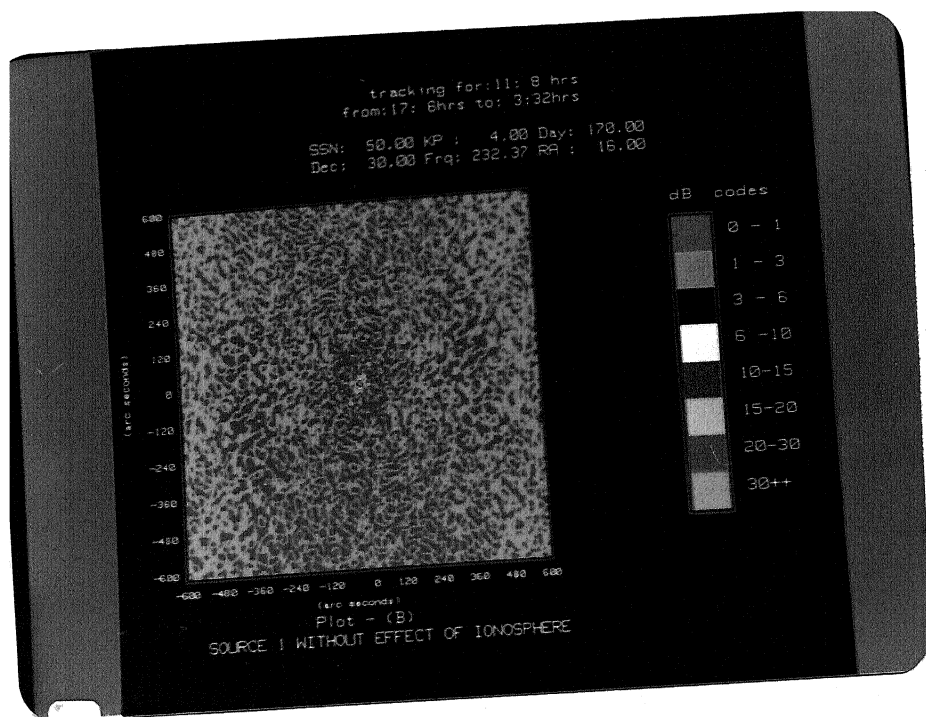


Fig. 5.14(a) : Plot-B corresponding to Plot-A of Fig. 5.1.

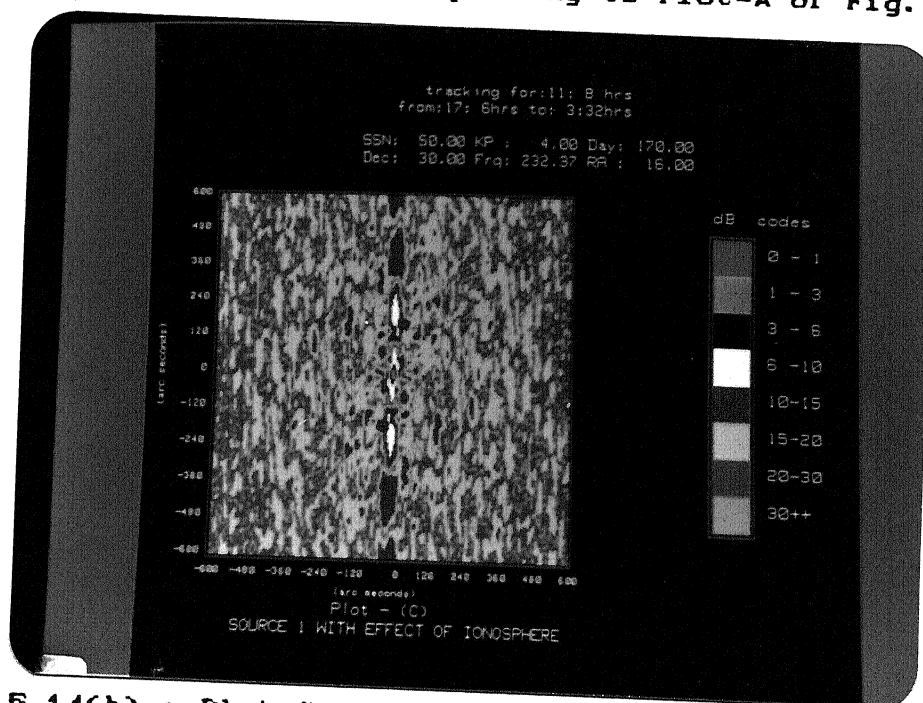


Fig. 5.14(b) : Plot-C corresponding to Plot-A of Fig. 5.1.

Region	A-B		A-C		B-C	
	max	rms	max	rms	max	rms
0-30"	3.0	1.1	5.0	2.0	2.0	1.1
0-60"	7.0	3.6	15.0	7.4	10.0	4.0
0-120"	18.0	7.1	26.0	14.9	17.0	8.5
0-300"	59.0	30.2	70.0	40.8	32.0	12.5
0-600"	72.0	37.5	85.0	47.2	32.0	12.2

Table 12 : dB Errors for Plots of Fig. 5.14

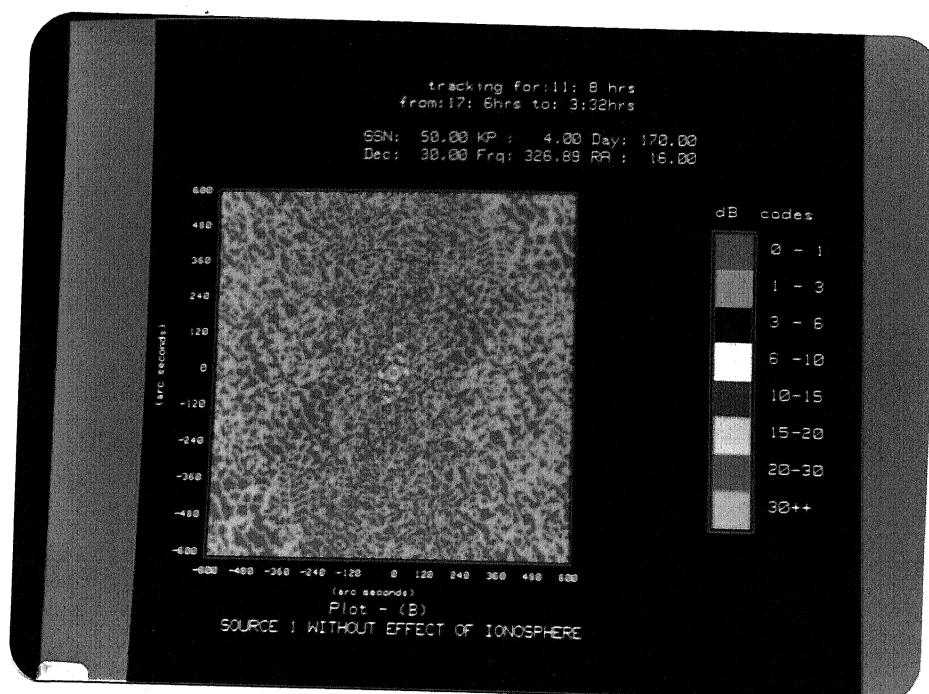


Fig. 5.15(a) : Plot-B corresponding to Plot-A of Fig. 5.1.

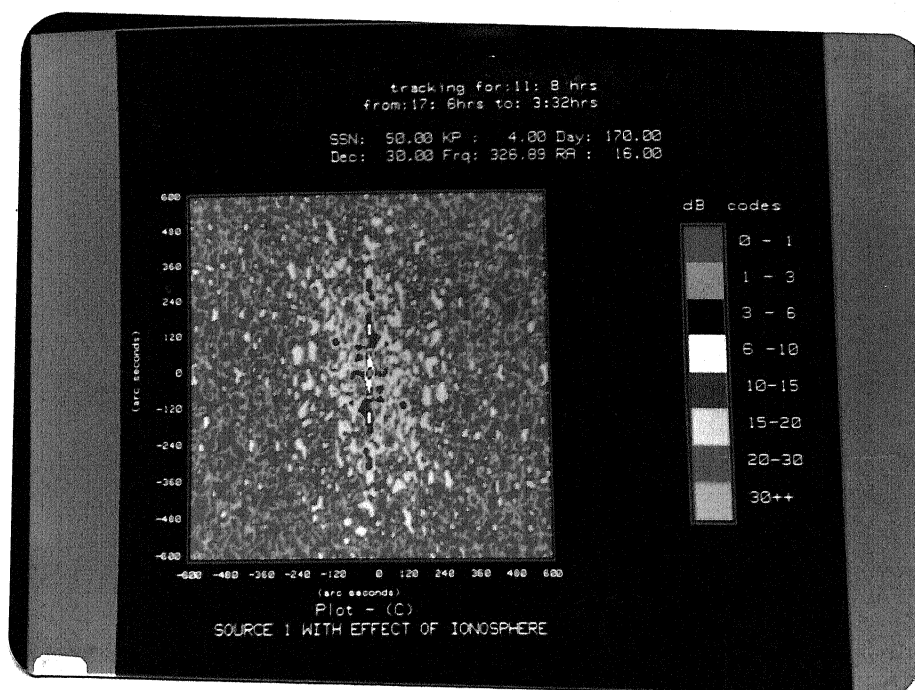


Fig. 5.15(b) : Plot-C corresponding to Plot-A of Fig. 5.1

Region	A-B		A-C		B-C	
	max	rms	max	rms	max	rms
0-30"	3.0	1.0	5.0	1.8	2.0	1.0
0-60"	7.0	3.7	14.0	6.6	8.0	3.2
0-120"	13.0	6.9	24.0	13.2	25.0	7.9
0-300"	60.0	31.0	66.0	39.0	26.0	10.8
0-600"	75.0	39.8	82.0	44.7	32.0	9.9

Table 13 : dB Errors for Plots of Fig. 5.15

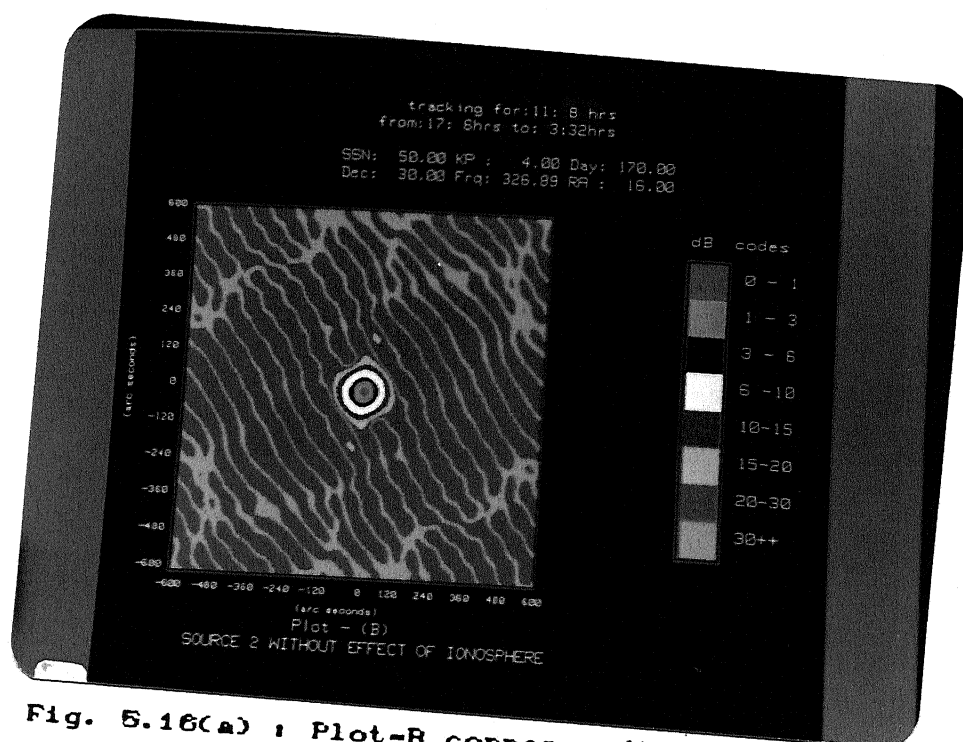


Fig. 5.16(a) : Plot-B corresponding to Plot-A of Fig. 5.2.

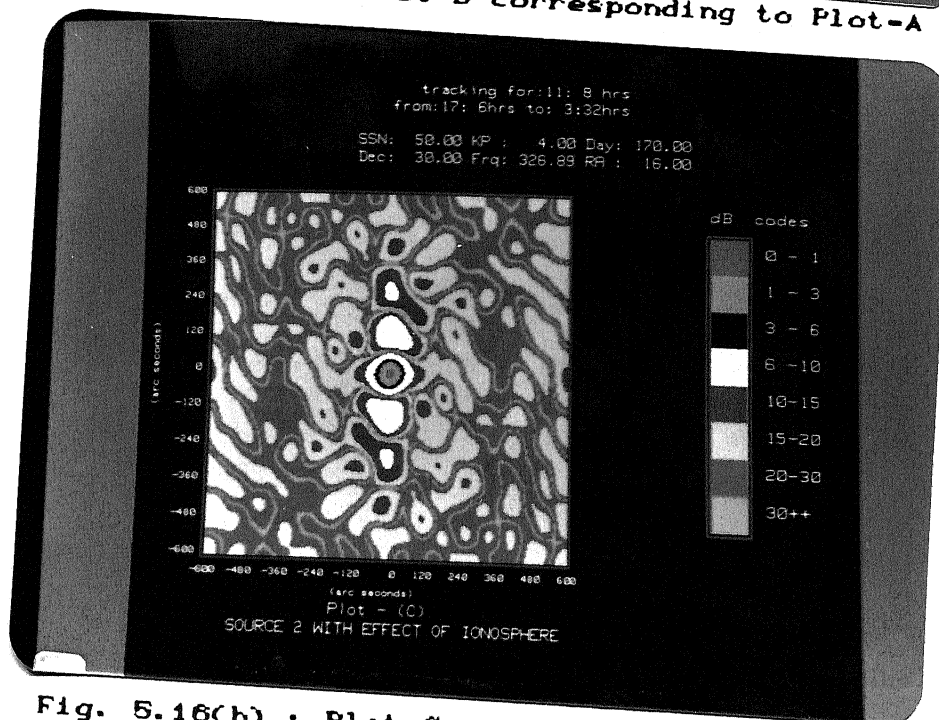


Fig. 5.16(b) : Plot-C corresponding to Plot-A of Fig. 5.2.

Region	A-B		A-C		B-C	
	max	rms	max	rms	max	rms
0-30"	0.0	0.0	0.0	0.0	0.0	0.0
0-60"	0.0	0.0	1.0	0.3	1.3	0.3
0-120"	0.0	0.0	1.0	0.2	1.2	0.2
0-300"	1.0	0.3	1.0	0.5	1.0	0.5
0-600"	1.0	0.5	1.0	0.7	1.0	0.5

Table 14 : dB Errors for Plots of Fig. 5.16

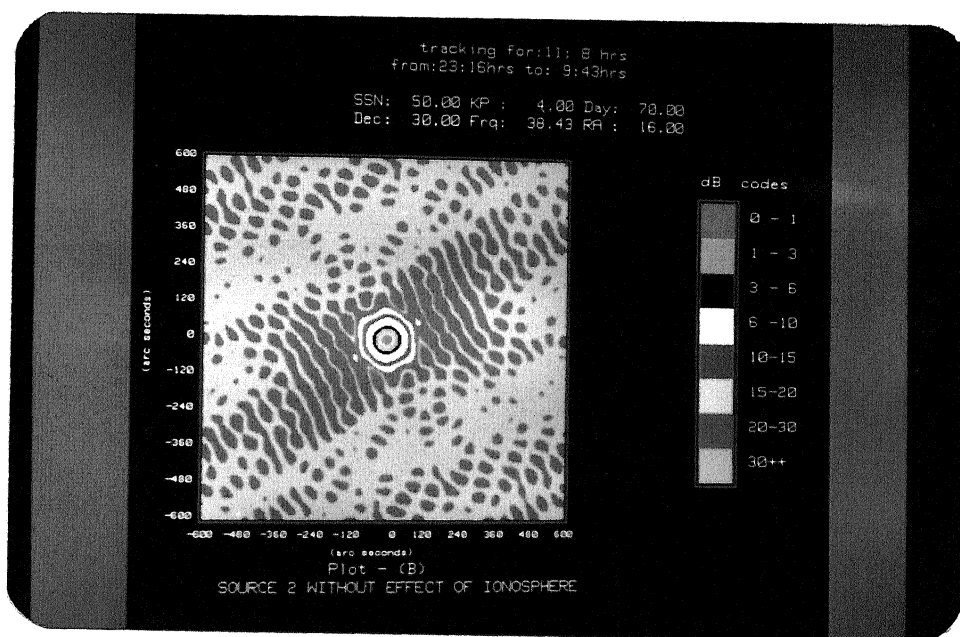


Fig. 5.17(a) : Plot-B corresponding to Plot-A of Fig. 5.2.

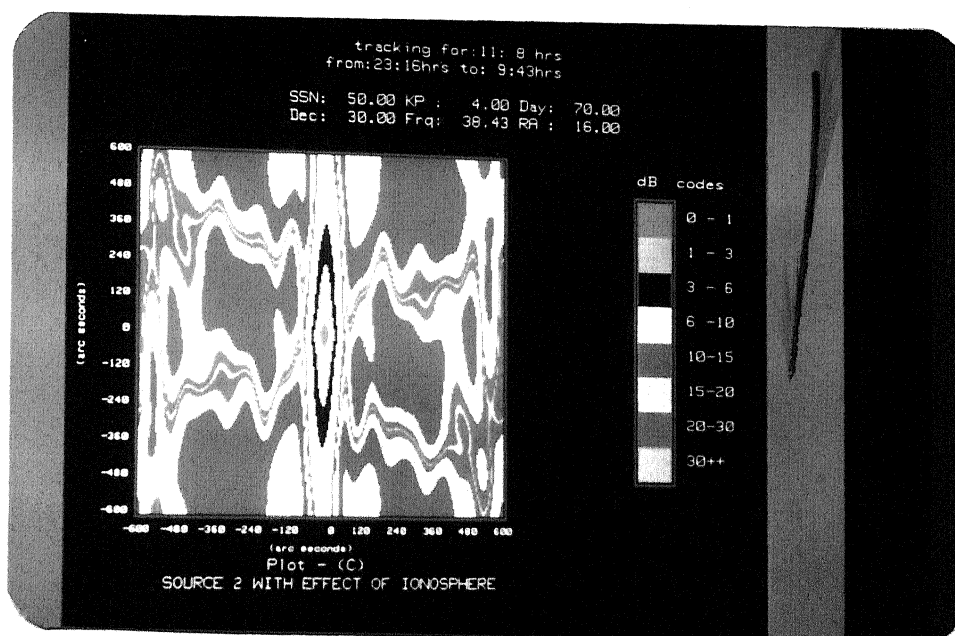


Fig. 5.17(b) : Plot-C corresponding to Plot-A of Fig. 5.2.

Region	A-B		A-C		B-C	
	max	rms	max	rms	max	rms
0-30"	0.0	0.0	0.0	0.0	0.0	0.0
0-60"	1.0	0.2	1.0	0.5	1.0	0.5
0-120"	1.0	0.2	1.0	0.7	1.0	0.7
0-300"	1.0	0.4	3.0	1.2	3.0	1.1
0-600"	1.0	0.5	5.0	2.2	5.0	2.0

Table 15 : dB Errors for Plots of Fig. 5.17

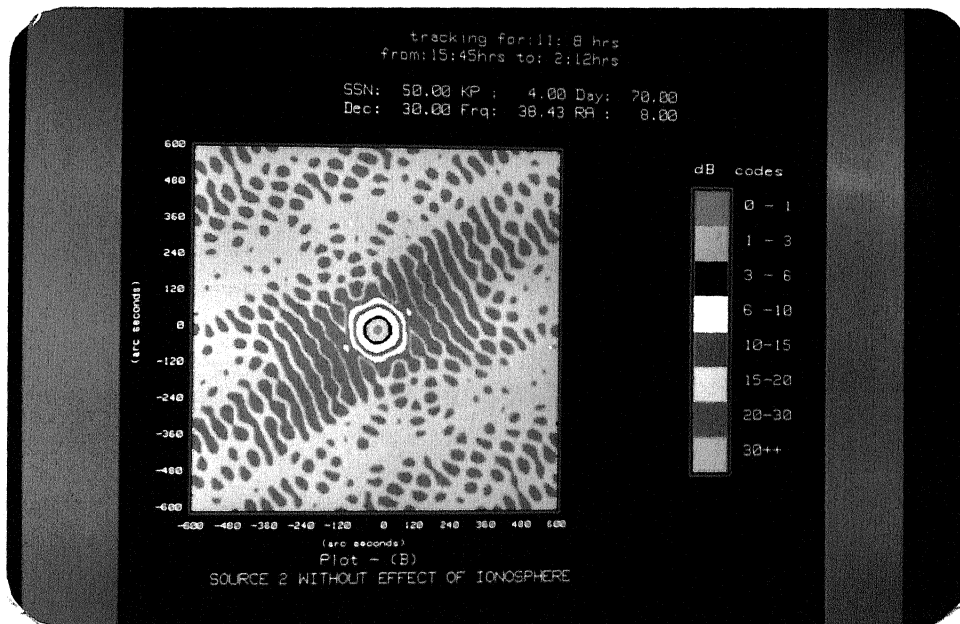


Fig. 5.18(a) : Plot-B corresponding to Plot-A of Fig. 5.2.

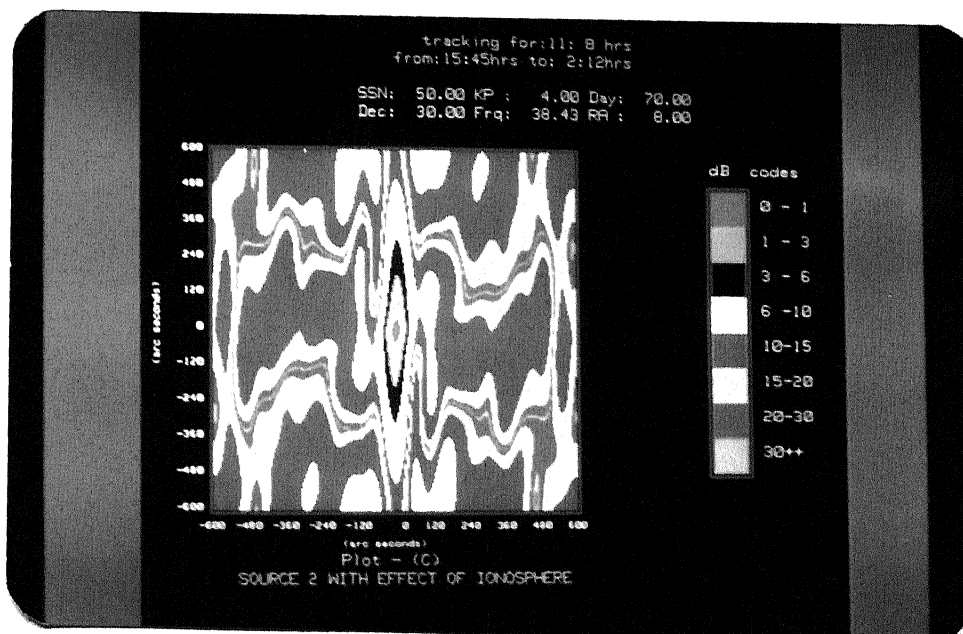


Fig. 5.18(b) : Plot-C corresponding to Plot-A of Fig. 5.2.

Region	A-B		A-C		B-C	
	max	rms	max	rms	max	rms
0-30"	0.0	0.0	0.0	0.0	0.0	0.0
0-60"	1.0	0.2	1.0	0.5	1.0	0.5
0-120"	1.0	0.2	1.0	0.7	1.0	0.6
0-300"	1.0	0.4	3.0	1.2	3.0	1.1
0-600"	1.0	0.5	5.0	2.1	5.0	2.0

Table 16 : dB Errors for Plots of Fig. 5.18

## REFERENCES

1. Aarons, J., (1982), 'Global Morphology of Ionospheric Scintillations', Proc. IEEE, vol. 70, pp 360-368
2. Basu et al., (1983), 'Topside electron densities and scintillations', J. Geophys. Res., vol. 88, pp 403-415
3. Bhattacharya, A. and Rastogi R.G., (1986), 'Phase scintillation due to equatorial F-region irregularities with 2-component power law spectrum', J. Geophys. Res., vol. 91, pp 11359-11364
4. Bhattacharya, A., and R.G. Rastogi, (1991), 'Structure of ionospheric irregularities from amplitude and phase scintillation observations', Radio Sci., vol. 26, No. 2, pp 439-449
5. Booker, H.G., J.A. Ratcliffe and D.H. Shinn, (1950), 'Diffraction from an irregular screen with applications to Ionospheric Problems', Philos. Trans. R. Soc. London A, vol. 242, pp 579-607
6. Booker, H.G., (1958), 'The Use of Radio Stars to Study irregular refraction of Radio Waves in the ionosphere', Proc. IRE, vol. 46, pp 298-314
7. Bramley, E.N., (1977), 'The accuracy of computing ionospheric radio wave scintillation by the thin phase screen approximation', J. Atm. Terr. Phys., vol. 39, pp 367-373
8. Crane, R.K., (1977), 'Ionospheric Scintillation', Proc. IEEE, vol. 65, pp 180-199
9. Davies, K., (1990), "Ionospheric Radio", Peter Peregrinus Ltd., London
10. Dyson, P.L., J.P. McClure, and W.B. Hanson, (1974), 'In situ measurements of the spectral characteristics of F-region ionospheric irregularities', J. Geophys. Res., vol. 79, pp 1497-1502
11. Evans, J.V. and T. Hagfors, (1968), "Radar Astronomy", McGraw-Hill, New York
12. Fejer, B.G., and M.C. Kelley, (1980), 'Ionospheric irregularities', Rev. Geophys. Space Sci., vol. 18, pp 401-454

13. Fomalont Edward B., (1978), "Image Formation from Coherence Functions in Astronomy", Edited by Cornelis van Schooneveld, D. Reidel Publishing Company, Chapter 1
14. Franke, Liu and Fang, (1984), 'Multifrequency study of ionospheric scintillation of Ascension Island', Radio Sci., vol. 19, pp 695-706
15. Fremouw, E.J. and J.A. Secan (1984), 'Modelling and Scientific application of scintillation results', Radio Sci., vol. 19, No. 3, pp 687-694
16. Hagfors, T., (1976), "Methods of Experimental Physics", vol. 12, part B, Chapter 2, edited by M.L. Meeks, Academic Press, New York
17. Hewish, A., (1952), 'The diffraction of galactic radio waves as a method of investigating the irregular structure of the ionosphere', Proc. Roy. Soc., vol. A214, pp 492-514
18. Ishimaru, A., (1978), "Wave propagation and scattering in Random Media," New York, Academic Press, vol. 1 & 2
19. Lawrence, R.S., C.G. Little, and H.J.A. Chivers, (1964), 'A Survey of Ionospheric effects upon earth space Radio Propagation', Proc. IEEE, vol. 52, pp 4-27
20. Lee, L.C., (1974), 'Wave propagation in a random medium : A complete set of moment equations with different wave numbers,' J. Math. Phys., vol. 15, pp 1431-1435
21. Mathur, N.C., (1969), 'A Pseudodynamic Programming Technique for the Design of Correlator Super-synthesis Arrays', Radio Sci., vol. 4, pp 235-244
22. Phelps, A.D.R. and R.C. Sagalyu, (1978), 'Plasma density irregularities in the high latitude topside ionosphere', J. Geophys. Res., vol. 81, pp 515-523
23. Ratcliffe, J.A., (1956), 'Some aspects of Diffraction theory and their application to the Ionosphere', Rep. Prog. Phys., vol. 19, pp 188-267
24. Rino, C.L. and Fremouw, E.J., (1977), 'The angle dependence of singly scattered wavefields', J. of Atm. & Terr. Phys., vol. 39, pp 859-868
25. Rino, C.L., (1978), 'Iterative methods for treating the multiple scattering of radio waves', J. Atm. Terr. Phys., vol. 40, pp 1011-1018

26. Rino, C.L., (1979), 'A power law phase screen model for ionospheric scintillation, 1. Weak scatter', Radio Sci., vol. 14, No. 6, pp 1135-1145
27. Rufenach, C.L., (1972), 'Power law wave number spectrum deduced from ionospheric scintillation observations', J. Geophys. Res., vol. 77, pp 4761-4772
28. Spoelstra, T.A.T., (1983), 'The influence of Ionospheric Refraction on Radio Astronomy Interferometry', Astron. Astrophys., vol. 120, pp 313-321
29. Spoelstra, T.A.T. and H. Kelder, (1984), 'Effects produced by Ionosphere on Radio Interferometry', Radio Sci., vol. 19, pp 779-788
30. Swarup, G. (1990), 'Giant metrewave radio telescope (GMRT) - Scientific objectives and design aspects', I.J. of Radio & Space Phys., vol. 19, pp 493-505
31. Tatarskii, V.I. (1971), 'The effects of turbulent atmosphere on wave propagation', Nat. Tech. Inform. Service, Springfield, VA
32. Thompson, A.R., J.M. Moran and G.W. Swenson Jr., (1986), "Interferometry and Synthesis in Radio Astronomy", John Wiley and Sons, NY
33. Umeki et al., (1977), 'Multifrequency spectra of Ionospheric Amplitude Scintillation', J. Geo. Res., vol. 82, No. 19, pp 2752-2758
34. Yeh., K.C. and Liu, C.H., (1982), 'Radio Wave Scintillations in the ionosphere', Proc. IEEE, vol. 70, pp 324-360